



TECHNISCHE  
UNIVERSITÄT  
WIEN

# Development and investigation of a finite-element model for predicting railway vehicle undefloor noise

Diplomarbeit  
**Likun LUO**



TECHNISCHE  
UNIVERSITÄT  
WIEN



## DIPLOMARBEIT

# Development and investigation of a finite-element model for predicting railway vehicle underfloor noise

ausgeführt zum Zwecke der Erlangung  
des akademischen Grades eines Diplom-Ingenieurs  
unter der Leitung von

Assistant Prof. Dipl.-Ing. Dr.techn. Florian Toth  
Institut für Mechanik und Mechatronik, E325-03

und

Dipl.-Ing. Michael Steinhauser  
Siemens Mobility Austria GmbH  
Leberstraße 34, A-1110 Wien

eingereicht an der Technischen Universität Wien  
**Fakultät für Maschinenwesen und Betriebswissenschaften**  
von

Likun LUO  
Matrikelnummer 11771106  
Wien, am 10. Jänner 2023

Unterschrift

## **Abstract**

## **Kurzfassung**

# Contents

<b>1</b>	<b>Introduction</b>	<b>1</b>
1.1	Background . . . . .	1
1.2	Aims and objectives . . . . .	2
<b>2</b>	<b>Fundamentals</b>	<b>3</b>
2.1	Governing equations and finite element formulation . . . . .	3
2.2	Perfectly Matched Layer . . . . .	3
2.3	Non-conforming grids . . . . .	3
2.4	Fundamentals of noise measurement . . . . .	3
2.4.1	Octave-band and fractional octave-band . . . . .	3
2.4.2	Sound Level . . . . .	3
2.4.3	Weighting . . . . .	3
2.5	UBX metro train . . . . .	3
<b>3</b>	<b>Measurements</b>	<b>4</b>
3.1	Characterisation of sound source . . . . .	4
3.2	Pressure field measurement on a standing metro train . . . . .	9
<b>4</b>	<b>Finite Element Modeling</b>	<b>18</b>
4.1	Geometry and mesh . . . . .	18
4.2	Boundary conditions and loads . . . . .	21
4.3	Parametric study . . . . .	24
4.3.1	Variation of underfloor geometry . . . . .	24
4.3.2	Inclusion of ground absorption . . . . .	24
4.3.3	Variation of frequency steps per 1/3-octave band . . . . .	26
<b>5</b>	<b>Results and Discussions</b>	<b>27</b>
5.1	Comparison of simulation and measurement results . . . . .	27
5.2	Effect of geometric variation . . . . .	31
5.3	Effect of ground absorption . . . . .	34
5.4	Effect of varying frequency steps per 1/3-octave band . . . . .	37
<b>6</b>	<b>Summary and future works</b>	<b>39</b>
<b>List of Figures</b>		<b>40</b>
<b>List of Tables</b>		<b>42</b>
<b>Bibliography</b>		<b>43</b>

## Notations and Symbols

$A$	$\text{m}^2$	Fläche ( <i>area</i> )
$c^D$	$\text{N}/\text{m}^2$	mechanischer Modul bei konstanter dielektrischer Verschiebung ( <i>stiffened elastic constant</i> )
$c^E$	$\text{N}/\text{m}^2$	mechanischer Modul bei konstanter elektrischer Feldstärke ( <i>elastic constant with constant E field</i> )
$c_s$	$\text{m}/\text{s}$	Schallgeschwindigkeit ( <i>wave velocity</i> )
$\bar{c}_s$	$\text{m}/\text{s}$	Steifigkeitsschallgeschwindigkeit ( <i>stiffened wave velocity</i> )
$c_l$	$\text{m}/\text{s}$	Longitudinalwellengeschwindigkeit
$c_t$	$\text{m}/\text{s}$	Transversalwellengeschwindigkeit
$\vec{T}_{\text{ges}}$	$\text{N}/\text{m}^2$	mechanische Spannung ( <i>stress</i> )
$\vec{T}$	$\text{N}/\text{m}^2$	mechanische Wechselspannung
$\vec{T}_e$	$\text{N}/\text{m}^2$	mechanische Wechselspannung der einfallenden Welle
$\vec{T}_r$	$\text{N}/\text{m}^2$	mechanische Wechselspannung der reflektierten Welle
$\vec{T}_d$	$\text{N}/\text{m}^2$	mechanische Wechselspannung der durchgehenden Welle
$\alpha$	$1/\text{m}$	Absorptionskoeffizient ( <i>attenuation constant</i> )
$\tilde{\gamma}$	dB	Absorptionsdämpfung
$\rho$	$\text{kg}/\text{m}^3$	Wechseldichte
$\tau$	s	Zeitverzögerung
$\Phi$	$\text{N}/\text{V}$	Wandlungsfaktor
$\frac{\partial \underline{x}}{\partial t}$		partielle Differentiation von $\underline{x}$ nach $t$
$\bar{x}$		Mittelwert von $x$
$\vec{x}$		Vektor $\vec{x}$
$\vec{x}_n$		Normalkomponente des Vektors $\vec{x}$
$\text{div } \vec{x}$		Divergenz des Vektors $\vec{x}$
$\nabla$		Nabla-Operator
$\mathbf{K}$		Matrix oder Tensor $\mathbf{K}$
$\mathbf{K}_t$		transponierte Matrix $\mathbf{K}$
$\underline{x}$		komplexe Zahl $\underline{x}$
$\text{Re}\{\underline{x}\}$		Realteil von $\underline{x}$
$\text{Im}\{\underline{x}\}$		Imaginärteil von $\underline{x}$
$\underline{x}^*$		konjugiert-komplex von $\underline{x}$
$j$		imaginäre Einheit
$J_n(x)$		Besselfunktion n-ter Ordnung

# Chapter 1

## Introduction

### 1.1 Background

Modern rail vehicles like trains, metro vehicles or trams have to meet ever increasing acoustic requirements and regulations not only to improve the acoustic comfort of the passengers, but also to reduce environmental noise pollution from railways [1–3].

The transmission of noises is complex procedures because many paths: airborne, structure borne structural vibration

- outline the specific objective of the research The aim of this thesis is ...

This thesis aims to provide/determine/develop/investigate

- Provide overview of thesis structure: The thesis is structured as follow ...

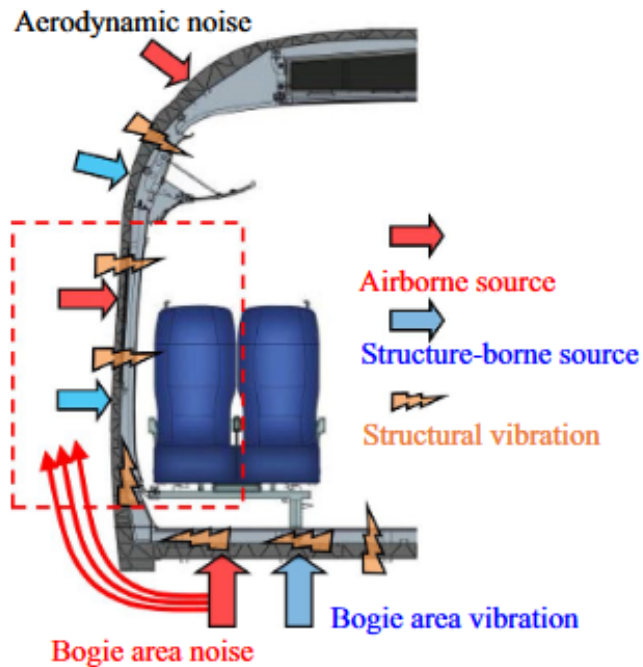


Figure 1.1: Transmission path of exterior noise sources [3]

## **1.2 Aims and objectives**

This thesis, in collaboration with Siemens Mobility Austria GmbH, aims to develop a finite-element model suitable for predicting the sound propagation from train underfloor area into the exterior environment around the carbody.

The thesis is organised as follows. The fundamental background of the thesis is explained in Chap. 2. Chap. 3 describes the outer pressure field measurement

# Chapter 2

## Fundamentals

2.1 Governing equations and finite element formulation

2.2 Perfectly Matched Layer

2.3 Non-conforming grids

2.4 Fundamentals of noise measurement

2.4.1 Octave-band and fractional octave-band

2.4.2 Sound Level

2.4.3 Weighting

2.5 UBX metro train

# Chapter 3

## Measurements

In order to be able to validate the results obtained from the latter finite element simulation, specific measurements have been carried out. In this chapter, the acoustic power measurement of sound source and the outer pressure field measurement around carbody are presented. The obtained sound power spectral of the omnidirectional loudspeaker provide simulation input for the finite element analysis in section 4.2. Furthermore, the measurement results of outer pressure field serve as validation for the finite element model in chapter 5.

### 3.1 Characterisation of sound source

Two important characteristics of a sound source are directivity and sound power. For the validation measurement, a dodecahedron loudspeaker of type Brüel & Kjaer 4292-L is used as excitation, which can be treated as an omnidirectional sound source. Hence, only the sound power emitted by the loudspeaker is of interest. In the following, the acoustic power spectrum of the sound source is measured following ISO 9614-2 [4].

#### Measurement setup

In fig. 3.1 the measurement setup for the determination of sound power levels is shown. The omnidirectional loudspeaker is placed on a concrete reflective floor and is enveloped by a 1m x 1m x 1m reference box. The loudspeaker is driven by a reference amplifier with pink noise as input signal (fig. 3.2). In order to reduce fluctuation in output power, the amplifier is switched on and warmed up for at least 20 minutes before the start of the measurement.

The measurement is carried out according to the ISO 9614-2 standard, in which the sound power is determined from intensity measurement over measurement surfaces. This method has the advantage that room reflections and any sound sources outside of the reference box do not influence the measurement result.

The intensity measurements are done using the Brüel & Kjaer sound intensity probe kit type 3654, which includes a pair of microphones that are placed face to face to each other, separated by a spacer. That is why this method of intensity measurement is also called two-microphone method or  $p-p$  method. Instead of direct measurement, the particle velocity is obtained by a finite-difference approximation to the pressure gradient. [5] [6]

From the euler equation of motion

$$\rho_0 \frac{\partial \vec{u}}{\partial t} = -\nabla p \approx -\frac{p_2 - p_1}{\Delta r} \quad (3.1)$$

where  $p_1$  and  $p_2$  are the measured pressure of the microphone closer and further from the incident sound wave, respectively and  $\Delta r$  the thickness of the spacer.

Hence, the particle velocity can be calculated from the two pressures

$$\vec{u} = \int \frac{(p_1 - p_2)}{\rho \Delta r} \partial t \quad (3.2)$$

The instantaneous sound intensity is obtained by the product of the approximated particle velocity and mean of the two measured pressures

$$\vec{I} = p\vec{u} = \frac{p_1 + p_2}{2} \int \frac{(p_1 - p_2)}{\rho \Delta r} \partial t \quad (3.3)$$

Fig. 3.3 shows the intensity measurement using scan method. For the scanning, the intensity probe is moved over the surface with a constant speed and is kept perpendicular to the scanned area so that only the normal component of intensity is captured:

$$I_n = \vec{I} \cdot \vec{n} \quad (3.4)$$

where  $\vec{n}$  is the unit normal vector of the measurement surface. Each partial measurement surface is scanned twice, using vertical and horizontal scan path, respectively. The obtained result is the spatial-averaged intensity. The sound power of a single measurement surface is given by the product of the spatial average intensity and the surface area:

$$W_i = \langle I_{ni} \rangle S_i \quad (3.5)$$

The total sound power of the enclosed sound source is given by:

$$W_{total} = \sum_{i=1}^N W_i \quad (3.6)$$



Figure 3.1: Setup for sound power measurement



(a) Inter-M R300 Plus reference amplifier

(b) NTI Minirator MR-PRO

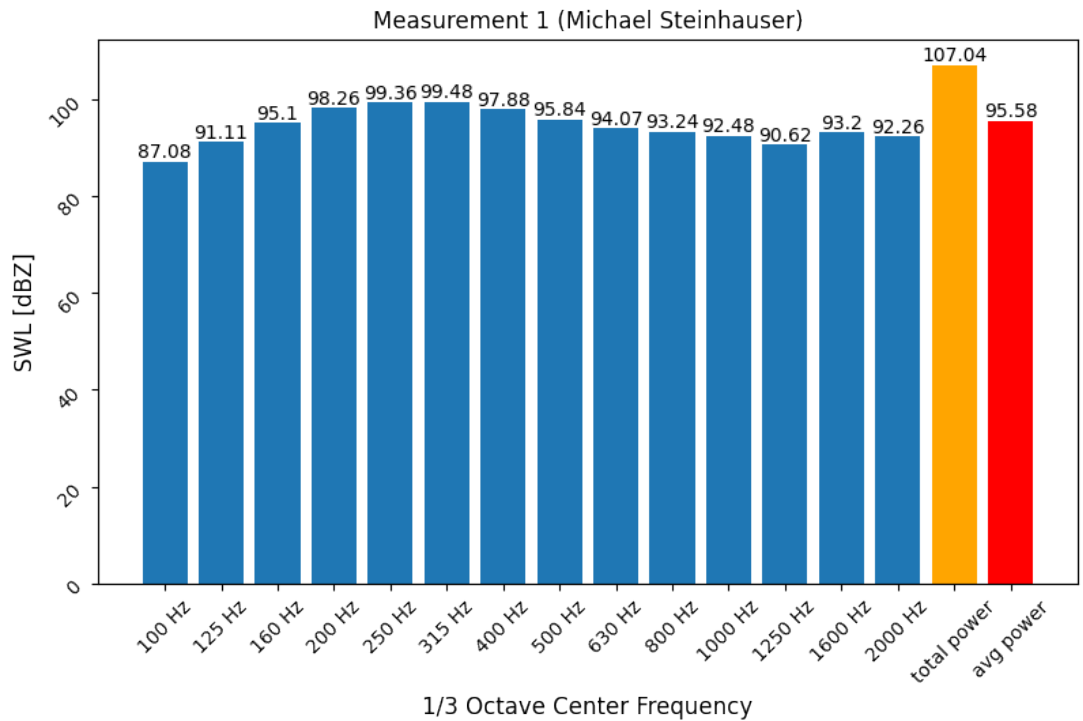
Figure 3.2: Signal generator and amplifier



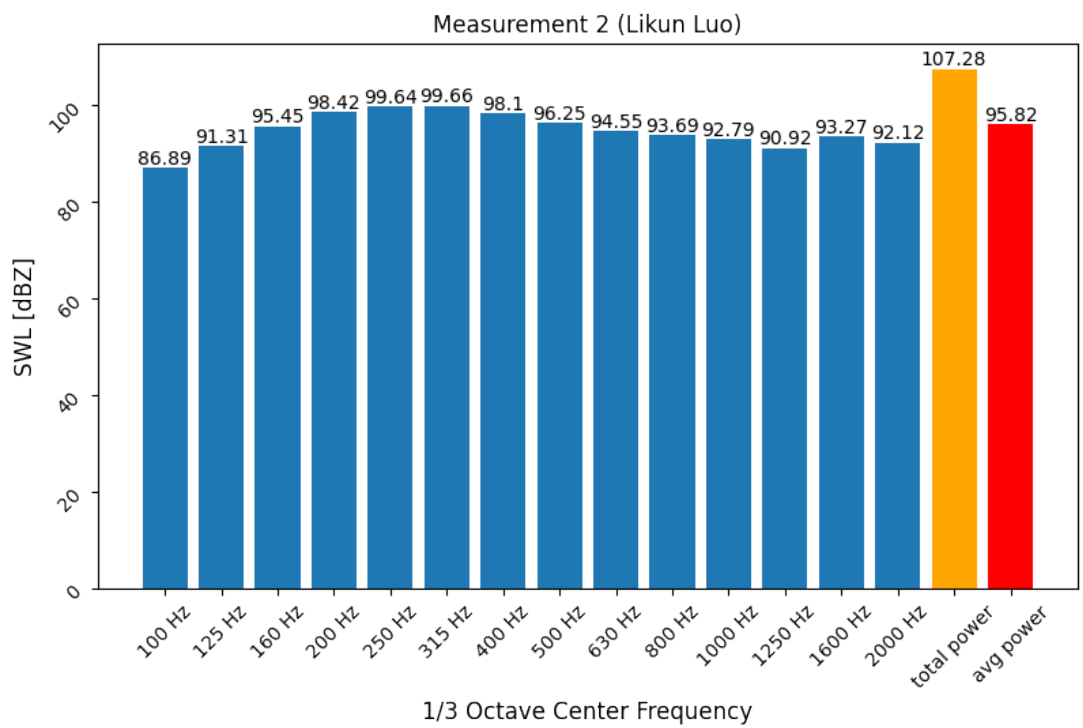
Figure 3.3: Scan method according to ISO 9614-2 [4]

## Measurement results

The measurement is post-processed using the Brüel & Kjaer type 2270 hand-held analyzer and the result is shown in one-third octave band spectra. Fig. 3.4 shows the measured nonweighted (Z-weighting) sound power level (SWL ref 1e – 12 W) from 100 Hz to 2000 Hz. The measurement is carried out twice, the deviation of both measurements is within 0.3 dB in total power. For the finite element simulation, the averaged value of both measurements as shown in fig. 3.4c will be used.



(a) Measurement series 1



(b) Measurement series 2

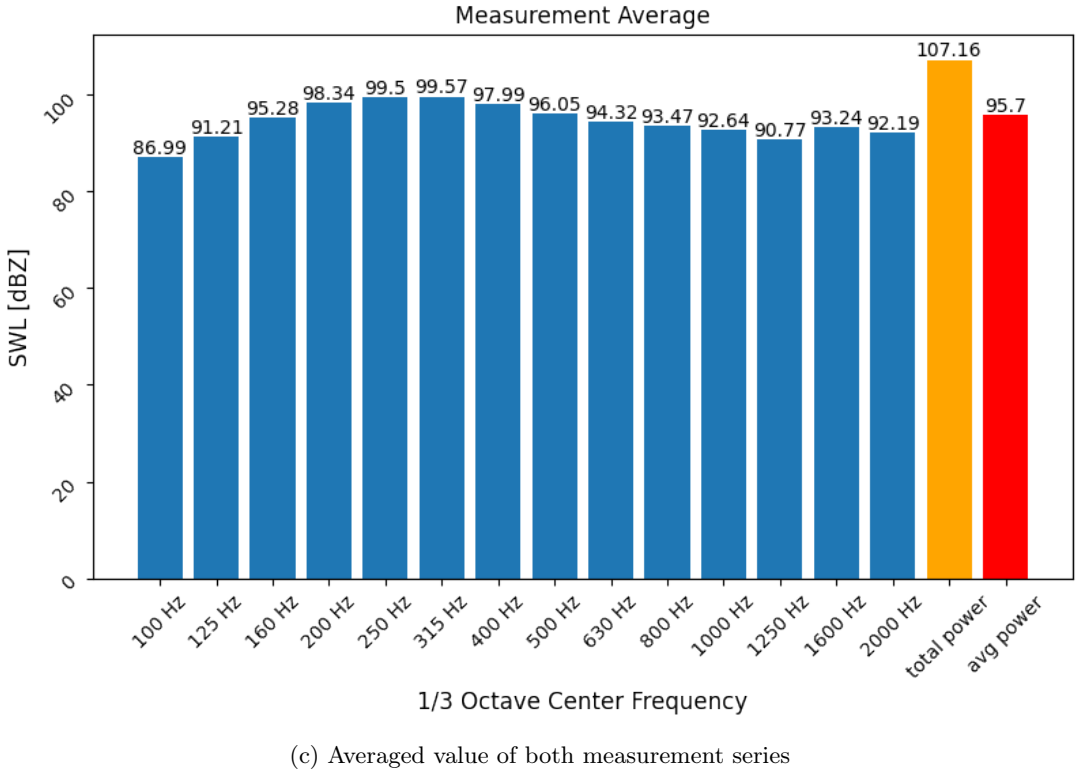


Figure 3.4: Sound power spectra in 1/3-Octave band

## 3.2 Pressure field measurement on a standing metro train

In this section, the sound pressure measurement on a standing UBX metro with controlled excitation has been carried out. The aim to perform measurements under standstill condition is to avoid the uncertainties introduced by the complex real sources (e.g. wheel-rail interaction) in dynamic conditions. In such wise, the quality of the finite element model can be better assessed.

### Measurement setup

The measurement was performed on October 4, 2022 at company premises of Siemens Mobility Austria in 1110 Vienna. The measurement setup is shown in fig. 3.5. Fig. 3.5a shows the front car of the measurement vehicle of type Siemens U-Bahn Wien X. In order to approximate free field conditions as closely as possible, the measurement vehicle is parked in a relatively empty area of company premises avoiding environmental reflections as much as possible.

To evaluate the outer pressure field close to the carbody, 10 pressure microphones are arranged in a line array order, allowing simultaneous measurement along the height direction. As shown in fig. 3.5b, the microphones are attached on a tripod at a distance of half meter to each other, the position of the microphones starts at 0.5 m and ends at 5 m above ground.

The acoustic excitation comes from an omnidirectional loudspeaker with pink noise as input signal, using the identical settings as in the previous acoustic power measurement. The loudspeaker is placed beneath the car underframe in the empty space between the bogie axle and the wheel axle, at about 55 cm above ground (Fig .3.6). Measurements have been performed with 2 different loudspeaker locations. One at the front of bogie (Position A), and the other at the rear (Position B), as marked in fig. 3.5b. The aim is to evaluate the possible asymmetric effect caused by the anti-symmetric layout of the bogie

components (e.g. brake discs), also it provides a validation for the latter finite element model, which will exploit the symmetry using image-source technique.

Due to the limited availability of the measurement vehicle, the measurement is concentrated on only one side of the vehicle, near the front bogie. In fig. 3.7, all measurement positions of the microphone array are shown and labeled. Position a is the starting position of measurement, it lies on the centerline of the bogie frame, 10 cm away from the carbody edge (Fig. 3.7b). The full description of measurement positions is found in the table below:

Position Label	Description
a	on bogie centerline , 10 cm away from carbody edge
b	50 cm out of bogie centerline in front direction, 10 cm away from carbody edge
c	100 cm out of bogie centerline in front direction, 10 cm away from carbody edge
d	50 cm out of bogie centerline in rear direction, 10 cm away from carbody edge
e	100 cm out of bogie centerline in rear direction, 10 cm away from carbody edge
f	on bogie centerline , 50 cm away from carbody edge
g	on bogie centerline , 100 cm away from carbody edge
h	on bogie centerline , 150 cm away from carbody edge
i	on bogie centerline , 200 cm away from carbody edge

Table 3.1: Description of measurement positions

At each measurement position, the multi-channel time-varying signal of the pressure field is captured by the Müller-BBM PAK MKII data acquisition system. The duration of single measurement run is set to 15 seconds. The captured time signal will be post-processed using the provided Müller-BBM PAK software suit.



(a) Front view



(b) Side view

Figure 3.5: Outer pressure field measurement setup

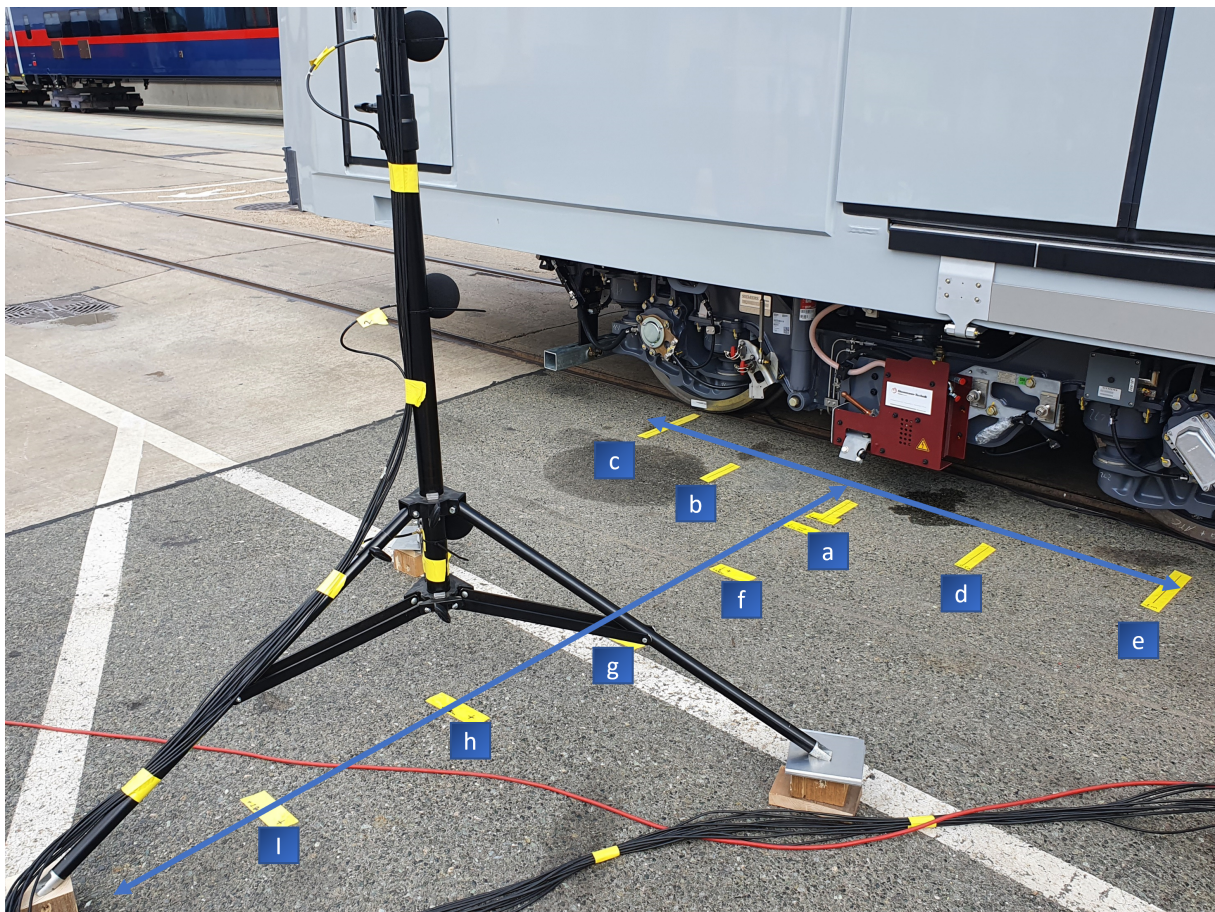


(a) Position A: front of bogie



(b) Position B: rear of bogie

Figure 3.6: Loudspeaker locations



(a) Measurement positions a to i



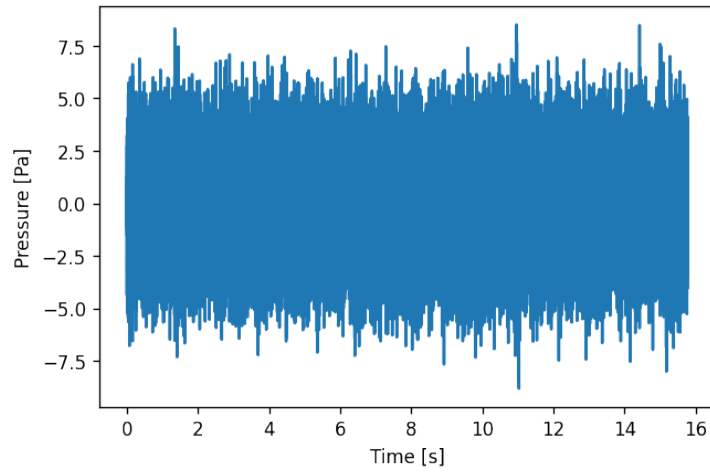
(b) Postition a: centerline of the bogie, 10 cm away from carbody edge

Figure 3.7: Measurement positions of microphone array

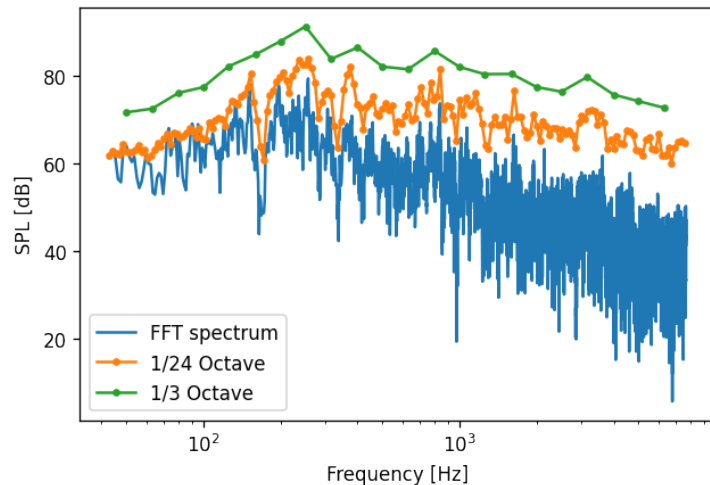
## Measurement results

In fig. 3.8a, the measured time signal of microphone 1 (0.5 m above ground) at measurement position a (front bogie centerline, 10 cm away from carbody) with loudspeaker placed at the front of bogie can be seen. The signal is converted into frequency domain using Fourier transformation as shown in fig. 3.8b. The post-processing can be done directly in the provided software suit Müller-BBM PAK 6.x, fig. 3.9 shows a screenshot of the GUI and the FFT parameter used is circled.

In fig. 3.8b, the blue curve shows the amplitude of acoustic pressure in narrow band resolution. The narrow band data is converted to 1/n octave form by summing up the amplitude of narrow-band spectral lines contained within the corresponding frequency bandwidth. The advantage of post-processing the data into octave bands is that it provides clearer information about the frequency composition of the noise signal. For example, it can be observed that in the 1/3 octave curve in fig. 3.8b, the peak of the SPL appears at 315 Hz, which also matches the peak in the SWL spectrum of the sound source as shown in fig. 3.4c.



(a) Time domain



(b) Frequency domain

Figure 3.8: Measurement data at position a, microphone 1 (0.5 m), loudspeaker front

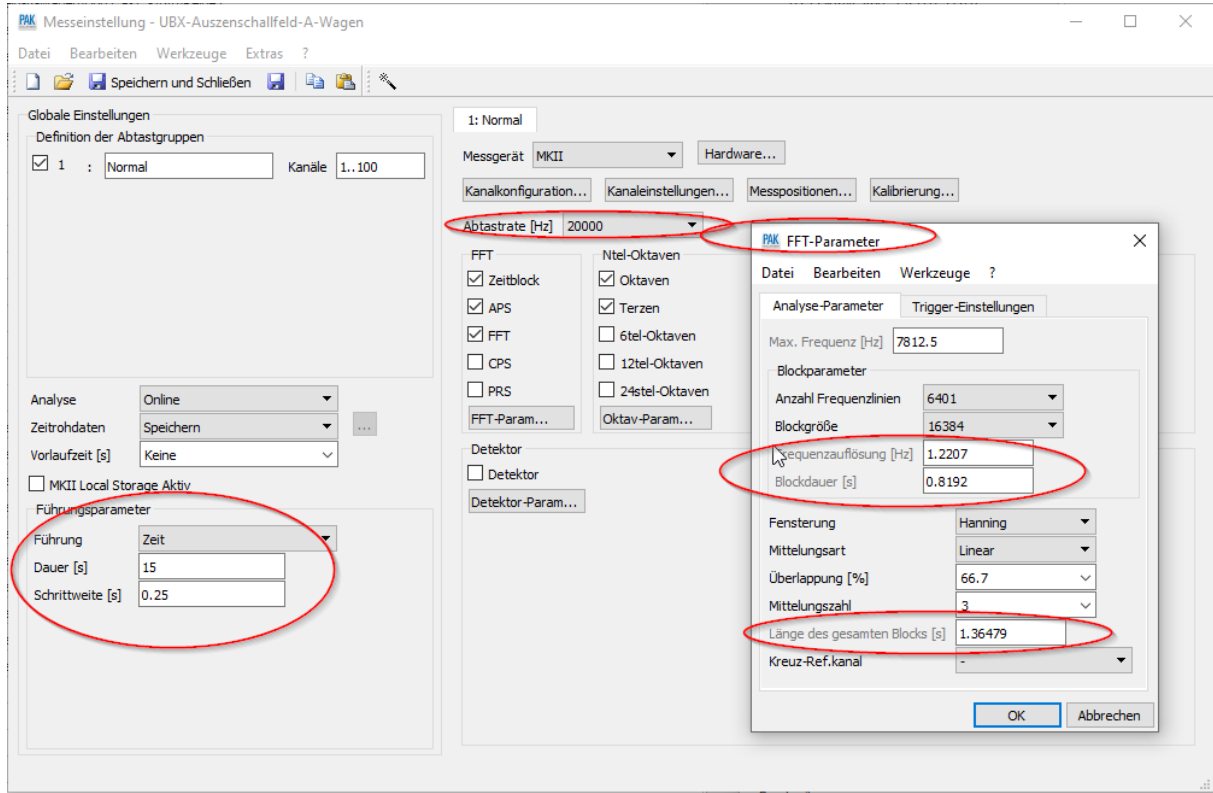


Figure 3.9: FFT parameter used

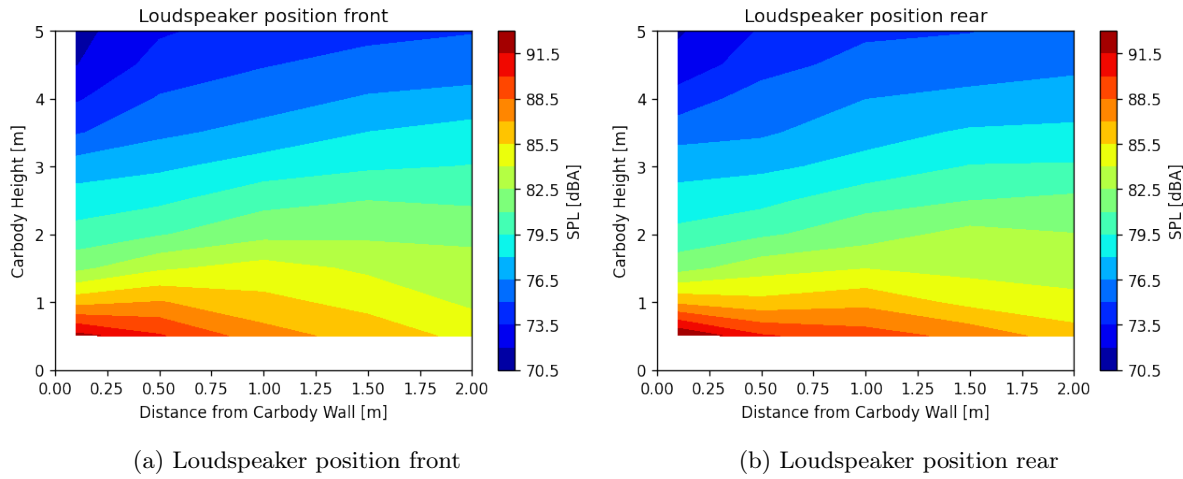


Figure 3.10: Pressure field around carbody

In fig. 3.10, a visualization of the total pressure field around the carbody is shown. The horizontal axis represents the distance from carbody wall, the vertical axis the height above ground and the color the a-weighted total pressure level, respectively. The white space in the plot is due to the missing data in the measurement since the measurement positions start at 10 cm away from carbody wall and half meter above ground. Comparing the pressure field of the two different loudspeaker locations, the asymmetric effect introduced by the brake disc can be observed. The brake disc of the front wheel axle standing in the transmission path of the loudspeaker seems to block a part of the acoustic wave.

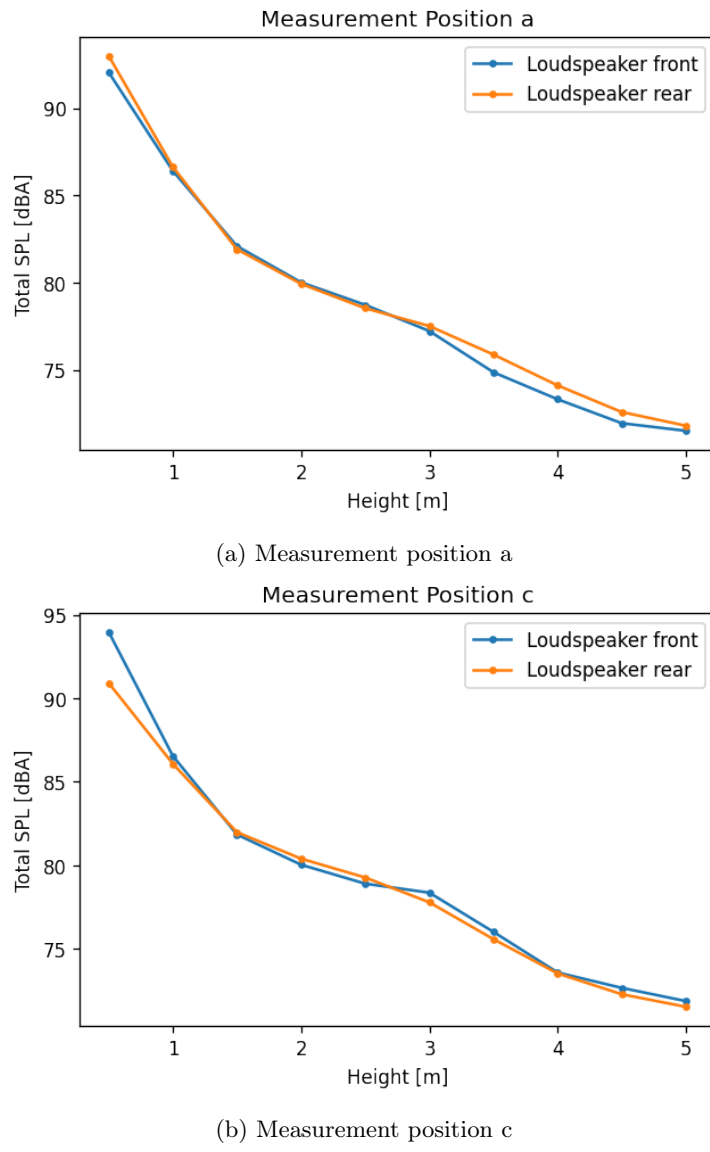
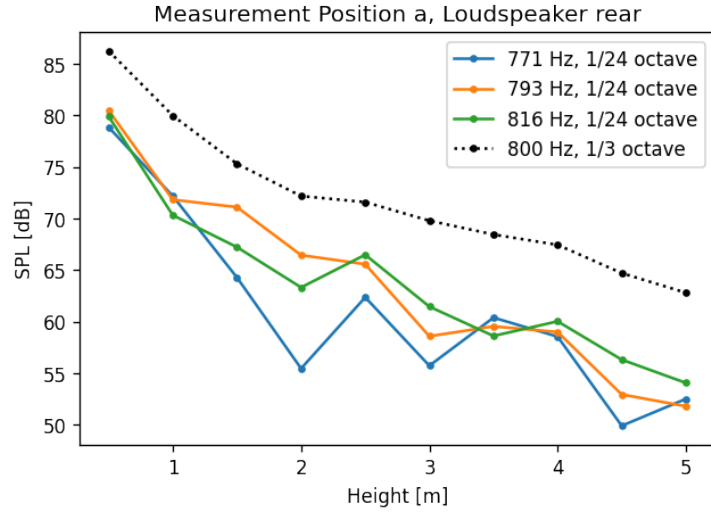
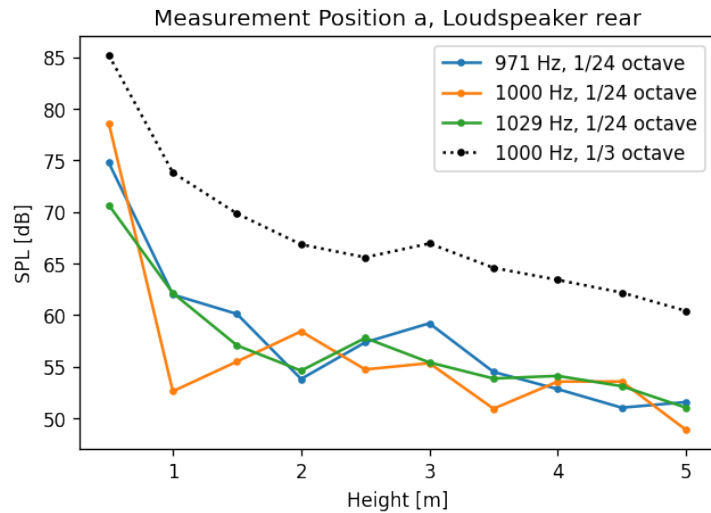


Figure 3.11: Total SPL as a function of the height above ground

In order to compare the pressure field quantitatively, one can plot the acoustic pressure as function of height for different measurement positions, which can be seen in the figures above. In 3.11a it can be observed that at measurement position a, the pressure curve caused by loudspeaker at different locations shares similar shape, and the pressure is strictly decreasing over carbody height.



(a) 800 Hz



(b) 1000 Hz

Figure 3.12: SPL as a function of the height above ground, single-frequency, measurement position a, loudspeaker rear

In fig. 3.12, the sound pressure level over height for different  $1/n$  octave band center frequencies is displayed. In the  $1/24$  octave resolution, several local minima in the curve shape can be observed, e.g. for 771 Hz in fig. 3.12a or for 1000 Hz in fig. 3.12b, which are caused by the destructive interference of the acoustic wave. The destructive interference can also be observed in the pressure field of the single frequency band as shown in fig. 3.13, sinks in acoustic field are to be found at about 1 m and 3.5 m height, respectively, which correspond to the position of the local minima in fig. 3.12b.

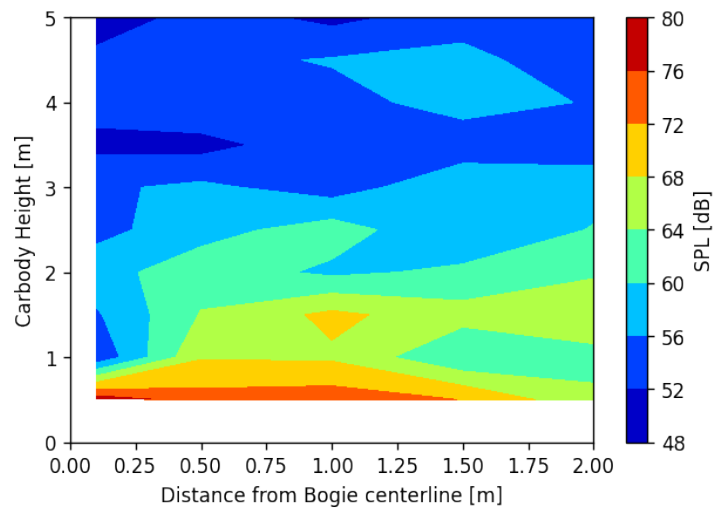


Figure 3.13: Pressure field of 1/24-octave frequency 1000 Hz, loudspeaker rear

# Chapter 4

## Finite Element Modeling

This chapter outlines the development of the finite element model of the UBX metro and the simulation setup. First, in section 4.1, the design of the model geometry and the mesh of the model are shown. Consecutively, section 4.2 describes the incorporation of boundary conditions into the finite element model. Finally, in section 4.3, a parametric study is carried out to investigate the influence of different simulation parameters on the solution of the initial finite element model. All these simulations are executed with the acoustics module of the open-source FEM software openCFS [7].

### 4.1 Geometry and mesh

Due to the large dimension of the car body, the computation of the complete model would be too extensive. Hence, the simulation model constitutes of the front bogie part only. The latter has been marked through a red box in fig. 4.1. Furthermore, the outer pressure field measurement described in sec. 3.2 has been taken from the same area.

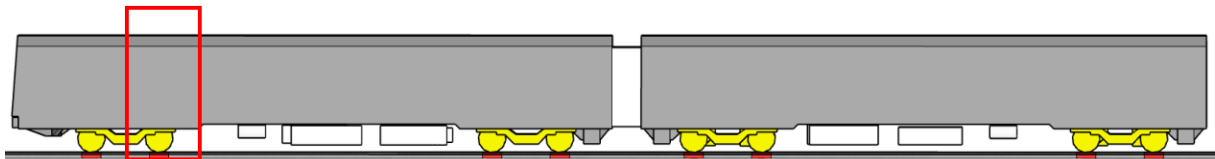


Figure 4.1: Side view of UBX, red box indicates the modeling area

In order to reduce computational effort, the symmetry of the model is exploited. The quarter model is depicted in fig. 4.2a, whereas the equivalent model, namely the full model, is shown in fig. 4.2b. Both models are shown for more comprehensive illustration of the modeled underfloor components, but only the quarter model has been used in the simulation. For simplification of the geometry design, exclusively the most essential components have been included in the model. Starting with the squared car body (dark green), the bogie (purple), the wheel (pink), the air suspension (gray) and ending with the omnidirectional loudspeaker (bright green). This respective component has been placed underneath the car floor, between bogie and the wheel axle and is represented through a sphere with 35 cm diameter.

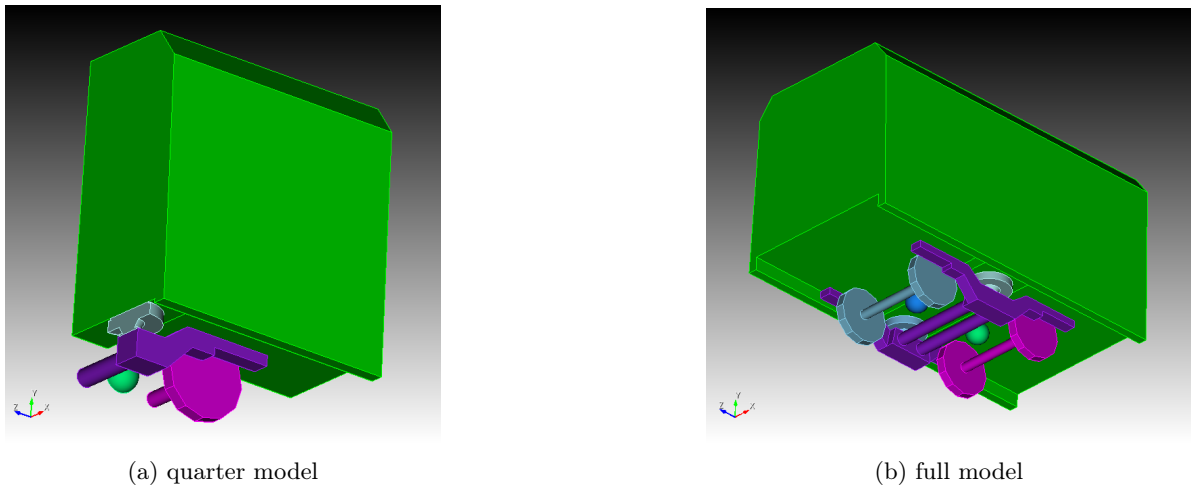


Figure 4.2: Geometry of model

The quarter model has been cut out from an acoustic region, surrounded by a perfectly matched layer to simulate the free field condition.

is surrounded by pml to model the open infinite domain

A mesh has been created from the 3d model.

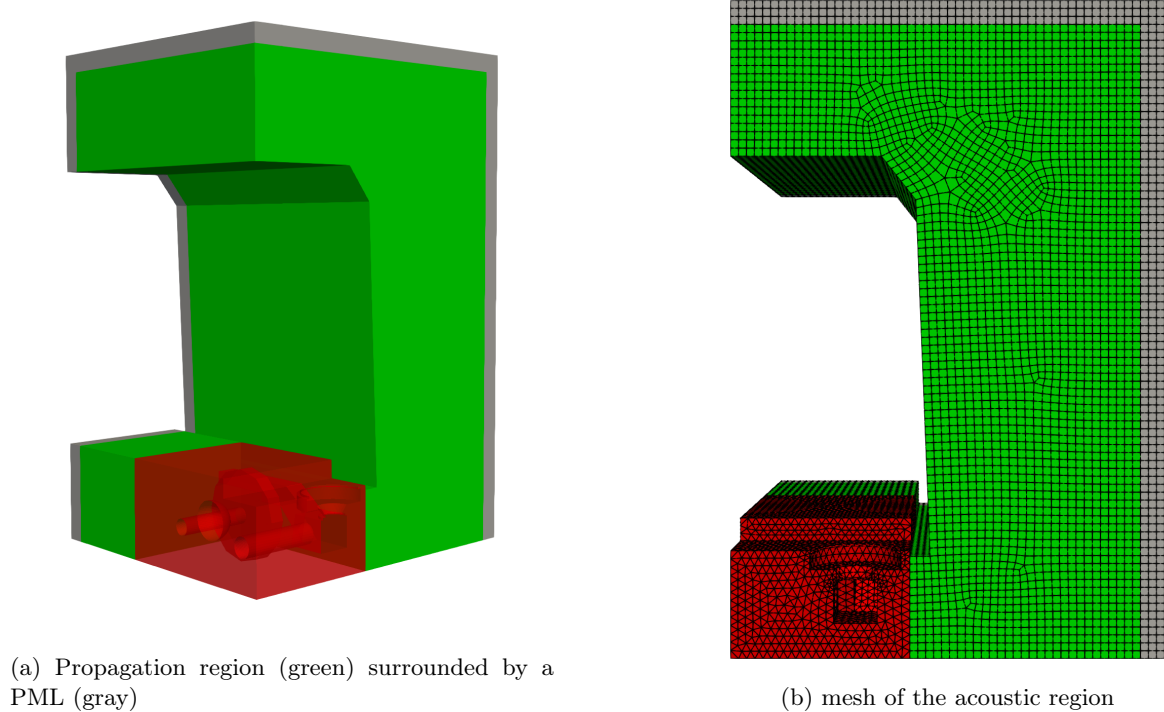


Figure 4.3: Acoustic region

## Determination of simulation domain

The goal of this section is to find an appropriate propagation domain size to achieve sufficient numerical accuracy while keeping the computational effort low. For the variation, the length and height of the propagation domain are kept constant while only the width of the domain is varied.

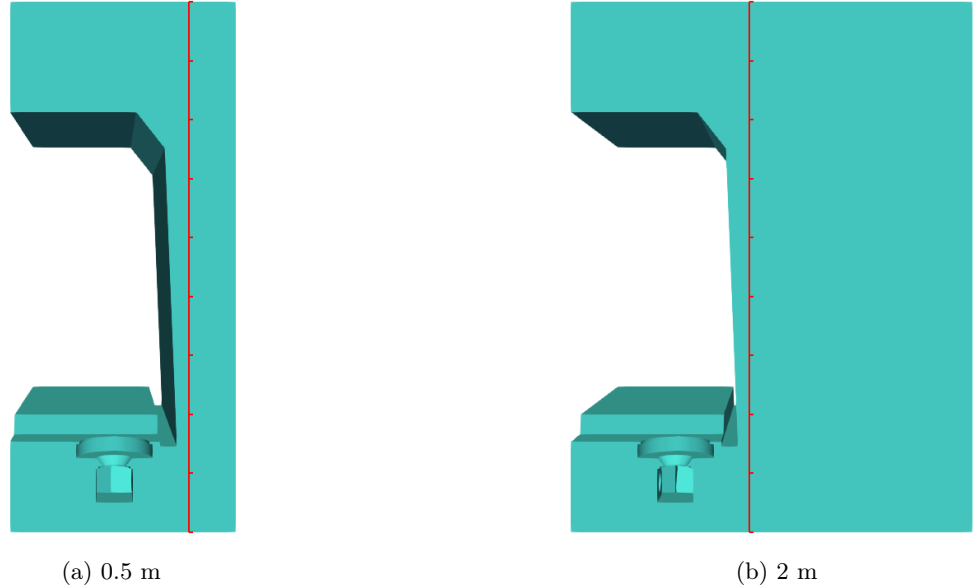


Figure 4.4: Models with different simulation domain size

The compared simulation domain size are 0.2 m, 0.5 m, 1 m, 1.5 m and 2m. For each setup, the pressure is evaluated at 0.1 m away from the vehicle along the height direction, and the result is compared to a , the model with 2 m domain size will be used as reference. Fig. 4.4 shows the model with 0.5 m domain size and the reference model with 2 m domain size. The evaluation position is marked by the red line.

## Computational Effort

The aim of this section is

Table 4.1: Computational effort for different 1/3-octave frequency band

1/3-octave center frequency (Hz)	Lower/upper frequency (Hz)	Mesh used	Degree of freedoms	Memory requirement (GB)	Solve time per 9 harmonic steps (hour)
100	89/112	1000 Hz 1.5 m	0.8 Million	20	0.5
125	112/141				
160	141/178				
200	178/224				
250	224/283				
315	283/356				
400	356/449				
500	449/565				
630	565/713				
800	713/897				
1000	897/1131	1600 Hz 1 m	2.3 Million	70	2
1250	1131/1425				
1600	1425/1796				
2000	1796/2262	2300 Hz 1 m	4.4 Million	150	5.5
			6.6 Million	260	12

## 4.2 Boundary conditions and loads

After the considerations of the geometrical model, the physical modeling aspects will be discussed. The dominating boundary condition in the finite element model of UBX is the Neumann type boundary condition, which specifies the acoustic particle velocity at the boundary.

The concrete ground  $\Gamma_{\text{ground}}$  and the wrapped surfaces of the vehicle components  $\Gamma_{\text{vehicle}}$  are assumed to be fully reflective. This also applies to the both symmetry planes (X-Y and Z-Y plane) of the quarter air domain  $\Gamma_{\text{symmetry}}$ . Hence, the sound hard boundary condition is used for these surfaces

$$\nabla p \cdot \vec{n} = 0 \quad \text{on} \quad \Gamma_{\text{ground}} \cup \Gamma_{\text{vehicle}} \cup \Gamma_{\text{symmetry}}. \quad (4.1)$$

To model the infinite domain, the three open surfaces of the propagation domain are surrounded by perfectly matched layers.

A familiar example of a normal velocity boundary is a vibrating mechanical structure that produces sound waves into the surrounding medium

Table 4.2: Material properties used for the simulation

Properties	Value
Density	$1.205 \text{ kg} \cdot \text{m}^{-3}$
Bulk modulus	$1.41767 \cdot 10^5 \text{ Pa}$

### Modeling of sound source

The loudspeaker sound source is modeled as a pulsating sphere radiating into free field, which is excited by a prescribed surface normal velocity  $\hat{u}(a)$  at source radius  $a$ .

The pressure amplitude of a spherical wave at radius  $r$  from the source is given by

$$\hat{p}(r) = \frac{A}{r} \cdot e^{-jkr}, \quad (4.2)$$

with  $A$  being the monopole amplitude and  $k$  being the wave number of the propagating wave.

The relationship between the pressure amplitude and the amplitude of particle velocity is described by the specific acoustic impedance, which is given by

$$z(r) = \frac{\hat{p}(r)}{\hat{u}(r)} = \rho_0 c_0 \frac{jkr}{1 + jkr}, \quad (4.3)$$

where  $\rho_0$  the density of the propagation medium and  $c_0$  the speed of sound in the medium. The product  $\rho_0 c_0 = z_0$  is also called the characteristic impedance of the propagation medium. (4.3) shows that for spherical wave, the acoustic pressure and the particle velocity are not in phase. For very small distances or low frequencies, phases differ by nearly  $90^\circ$  and in the acoustic far field ( $kr \gg 1$ ), the spherical wave can be approximated by plane wave propagation.

For stationary sound field, the average power density or sound intensity is given by

$$\bar{I}(r) = \frac{1}{2} \operatorname{Re}\{\hat{p}(r)\hat{u}^*(r)\} \quad (4.4)$$

$$= \frac{1}{2} \frac{|A|^2}{r^2 z_0}. \quad (4.5)$$

The acoustic power of a steady sound source radiating into free field is obtained by integrating the

sound intensity over a surface, which encloses the sound source and can be found as

$$W = \oint_{\Gamma} \bar{I}(r) d\Gamma \quad (4.6)$$

$$= \bar{I}(r) \cdot 4\pi r^2 \quad (4.7)$$

$$= \frac{2\pi|A|^2}{z_0} \quad (4.8)$$

As apparent in (4.8), the acoustic power is independent from the distance to the source.

With the goal of assessing the acoustic power  $W$ , an expression for the monopole amplitude  $A$  has to be determined and inserted into (4.8). On the surface of the source, the pressure is given by the product of the surface normal velocity  $\hat{u}(a)$  and the specific impedance  $z(a)$  evaluated at the source radius and is found by

$$\hat{p}(a) = \frac{A}{a} \cdot e^{-jka} = \hat{u}(a) \cdot z(a) \quad . \quad (4.9)$$

Upon bringing the monopole amplitude  $A$  to one side of the equation

$$A = a \cdot \hat{u}(a) \cdot z(a) \cdot e^{jka} \quad , \quad (4.10)$$

and inserting into (4.8), the acoustic power can hence be expressed by the surface normal velocity

$$W = 2\pi a^2 \cdot |\hat{u}(a)|^2 \cdot z_0 \cdot \frac{(ka)^2}{1 + (ka)^2} \quad . \quad (4.11)$$

After solving for  $|\hat{u}(a)|$

$$|\hat{u}(a)| = \sqrt{\frac{W \cdot (1 + k^2 a^2)}{2\pi z_0 k^2 a^4}} \quad (4.12)$$

the relationship between input surface normal velocity and the output acoustic power has been established. Through (4.12), the required surface normal velocity for a given source acoustic power can be calculated.

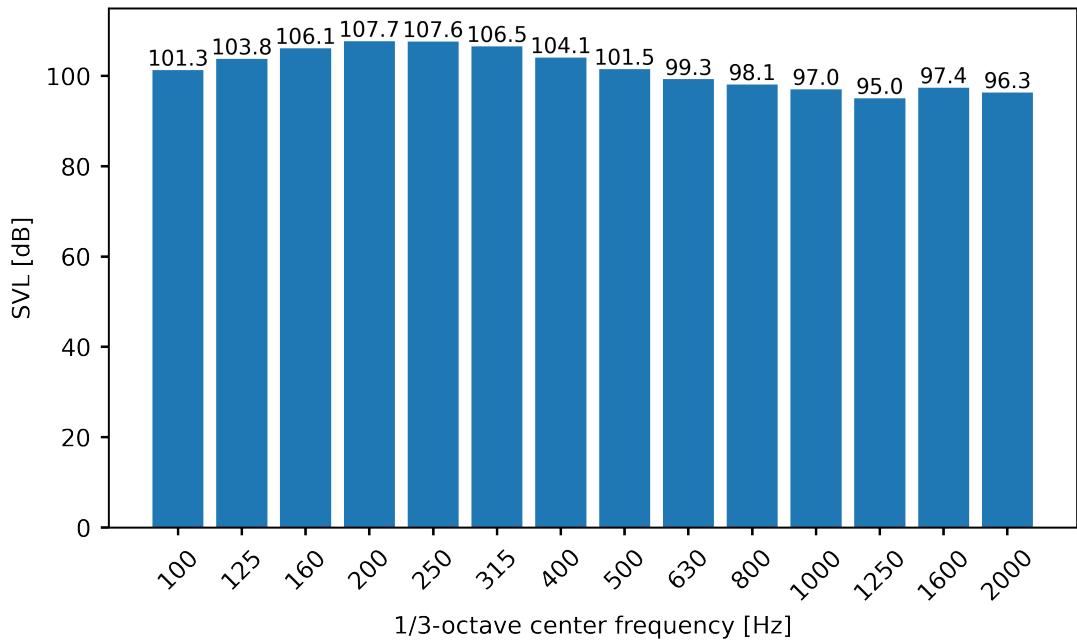


Figure 4.5: Input surface normal velocity in dB ref.  $5 \cdot 10^{-8}$  m/s, calculated using 4.12

For the simulation, the sound power level of one single 1/3-octave band is divided into the 9 intermediate frequency steps by a 9.54 dB reduced sound power level for every single frequency within the band so that the sum of all frequencies results in the sound power level for the corresponding 1/3-octave band.

## 4.3 Parametric study

### 4.3.1 Variation of underfloor geometry

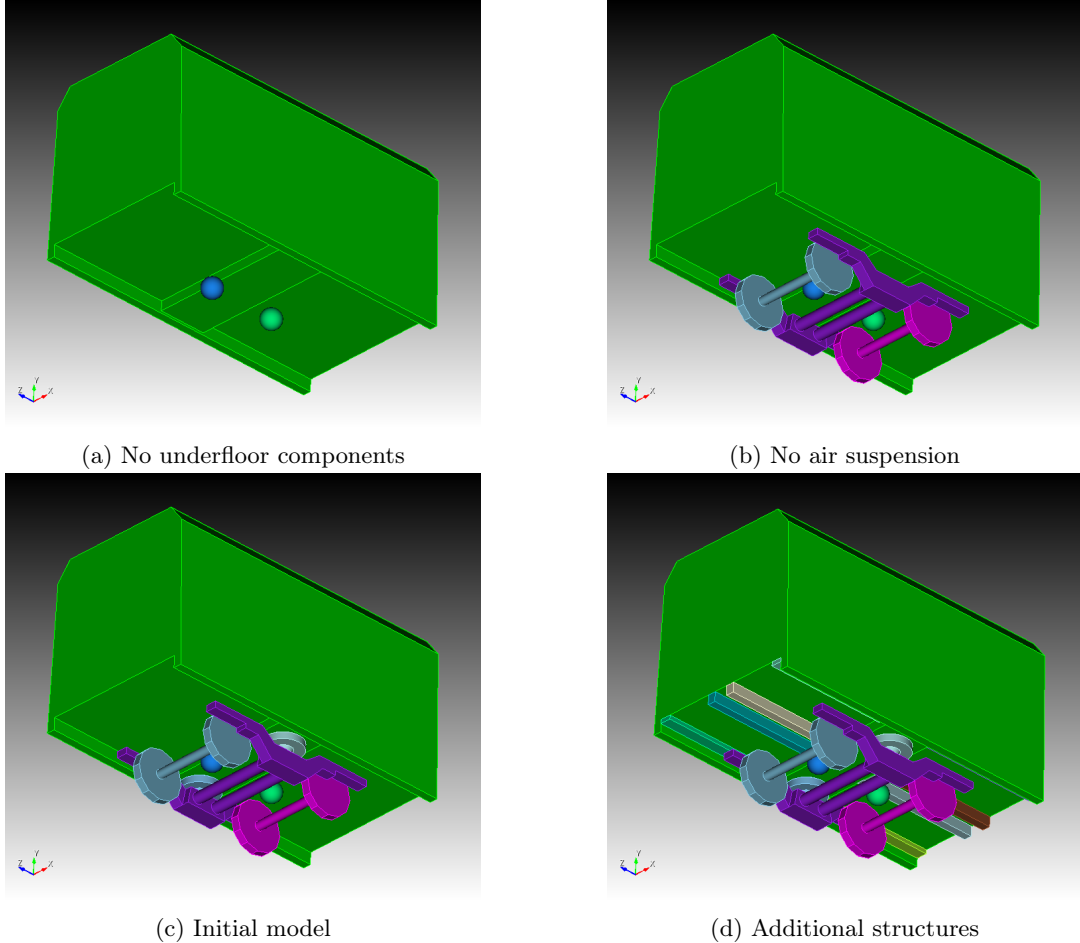


Figure 4.6: Used geometry

### 4.3.2 Inclusion of ground absorption

In the finite element formulation, the ground absorption is modeled by the surface impedance boundary condition. The surface impedance is complex valued. The phase information of the surface impedance is lost when converting to absorption coefficient. For most of the time, (in acoustic data bank) only the absorption coefficient is provided but not the full impedance characteristic. To have an idea how the missing phase information of the impedance could affect the results. It assumed that the phase of the surface impedance are  $0^\circ$ ,  $30^\circ$ ,  $45^\circ$  and  $60^\circ$ .

In the initial simulation setup, the ground is modeled as a perfect reflecting plane. To have an idea how the unknown

Due to a missing ground absorption measurement

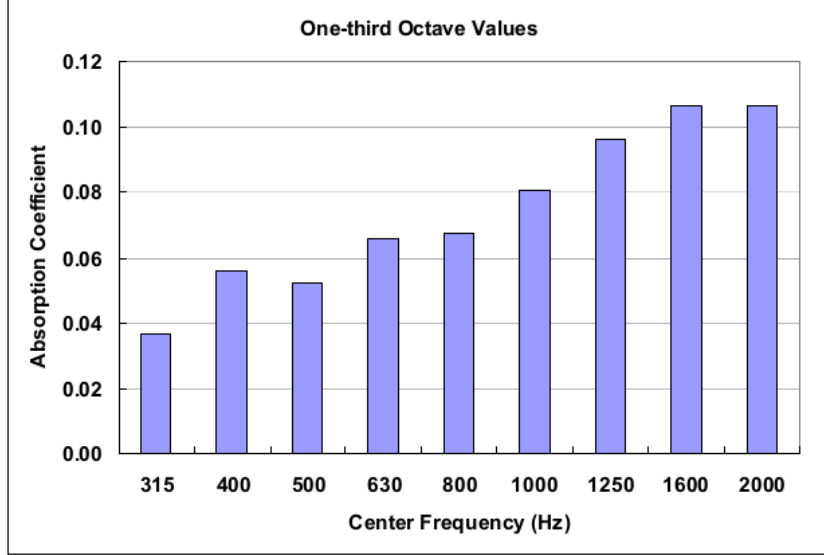


Figure 4.7: Absorption coefficient in one-third octave bands [8]

Table 4.3: Estimated absorption coefficient from fig. 4.7, the values for frequency lower than 315 Hz are chosen arbitrary

Freq (Hz)	100	125	160	200	250	315	400
$\alpha$	0.02	0.02	0.02	0.02	0.02	0.035	0.055

Freq (Hz)	500	630	800	1000	1250	1600	2000
$\alpha$	0.05	0.065	0.065	0.08	0.095	0.105	0.105

$$\alpha = 1 - |R^2| \quad (4.13)$$

$$R = \frac{Z_s - Z_0}{Z_s + Z_0} = \frac{\frac{Z_s}{Z_0} - 1}{\frac{Z_s}{Z_0} + 1} \quad (4.14)$$

$$\tilde{Z}_s = \frac{Z_s}{Z_0} = \tilde{R}_s + j\tilde{X}_s \quad (4.15)$$

$$\begin{cases} \frac{4\tilde{R}_s}{\tilde{R}_s^2 + \tilde{X}_s^2 + 2\tilde{R}_s + 1} = \alpha \\ \arctan \frac{\tilde{X}_s}{\tilde{R}_s} = \varphi \end{cases} \quad (4.16)$$

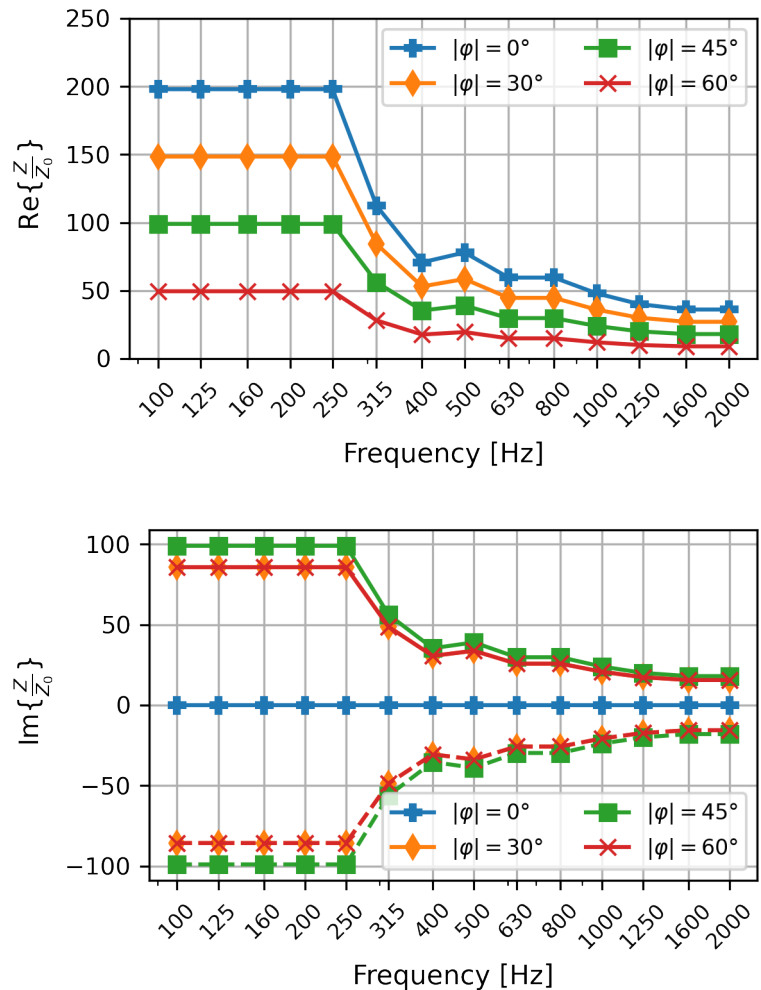


Figure 4.8: Input surface impedance in one-third octave bands calculated using (4.16)

#### 4.3.3 Variation of frequency steps per 1/3-octave band

# Chapter 5

## Results and Discussions

In the following, the results obtained from the finite element simulation using different setups are discussed and compared to the outer pressure field measurement.

### 5.1 Comparison of simulation and measurement results

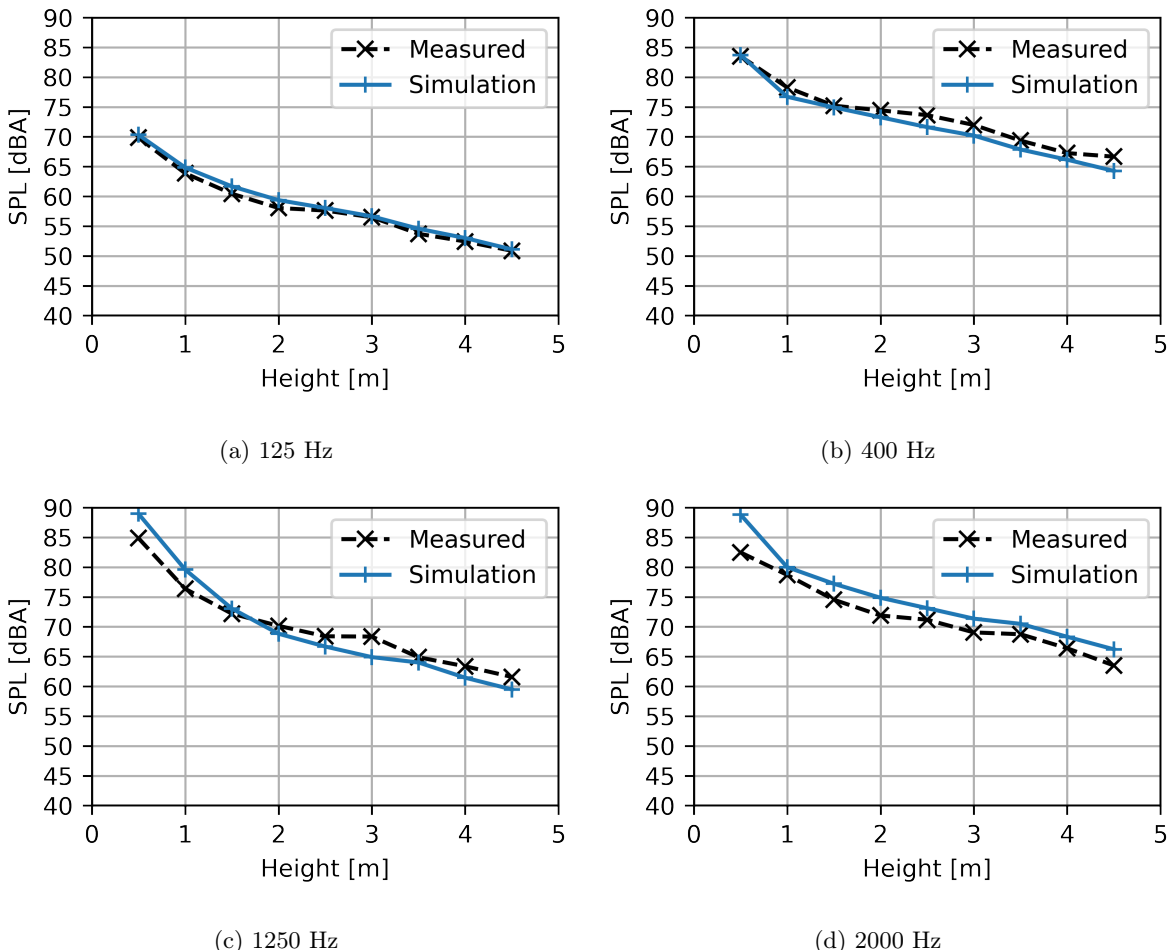


Figure 5.1: Sound distribution at measurement position a, comparison between predictions obtained from the initial finite element model with the measurements. A-weighted SPL in one-third octave bands, dBA ref 20  $\mu$ Pa.

In fig. 5.1, the A-weighted sound pressure levels at measurement position a (10 cm away from vehicle) along the car body height in example one-third octave bands are shown. At each microphone position, the simulation result is compared with the measurement value. One can see that for 125 Hz and 400 Hz, the simulation fits the measured curves very well. Greater difference between the simulation and the measurement occurs for 1250 Hz and 2000 Hz, but the measured shape is still well approximated for both frequency bands. Other bands show similar results and the measured sound pressure level trends are captured well by the model.

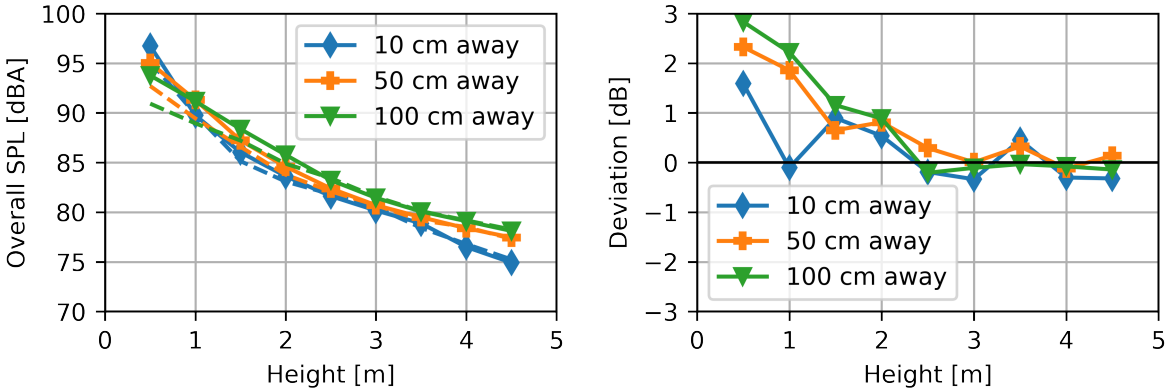
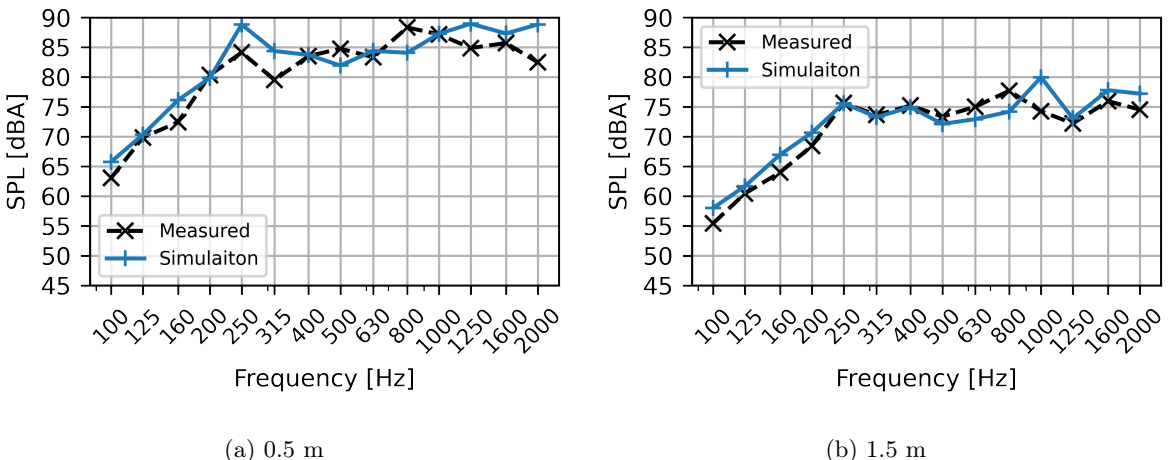
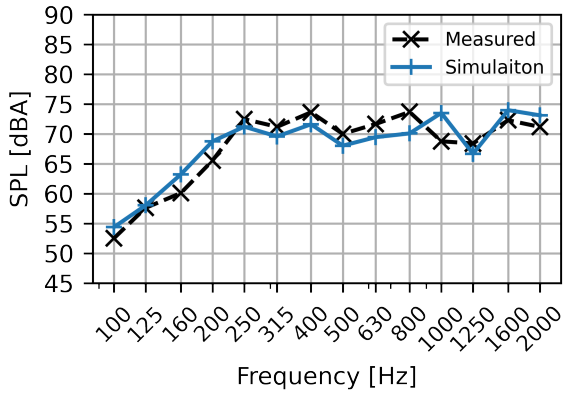


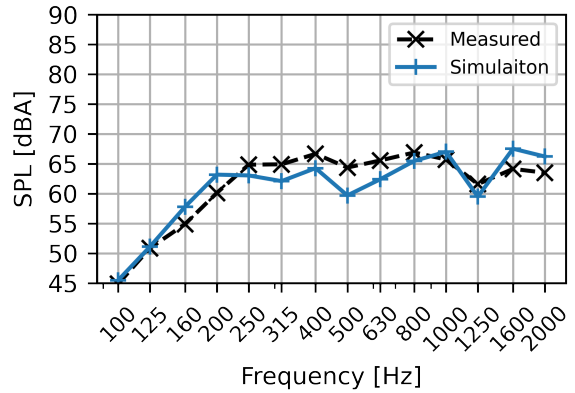
Figure 5.2: Comparison of overall SPL in dBA ref  $20 \mu\text{Pa}$ . Left: overall SPL as a function of height at various measurement positions (dashed curves: measurement; solid curves: simulation) Right: deviation between simulation and measurement results

The overall sound pressure level is a simple and direct parameter to quantify the sound level. For comparison, the A-weighted sound pressure levels of each one-third octave band from 100 Hz to 2000 Hz are added up. Fig. 5.2 shows the overall A-weighted sound pressure level at three different measurement positions and the deviation between the simulated and measured results. As can be seen from the results, the predictions of overall sound pressure levels at the three distances from car body agree well with the measurement. For all three measurement positions, the maximum deviation between the simulation and measurement results occurs at 0.5 m, which is at the height of the bogie. At these locations, the simulation results are overestimated by 1.5 dB to 3 dB. In general, the approximation is getting better with increasing height. For area above 2m, the difference between the simulation and the measurement in terms of overall sound pressure is within 1 dB.





(c) 2.5 m



(d) 4.5 m

Figure 5.3: 1/3-octave spectra of the A-weighted SPL for simulation and measurement data at selected microphone positions

Fig. 5.3 shows the spectra of the A-weighted sound pressure level in one third octave bands. The SPL spectra are evaluated at the measurement position a (10 cm away from vehicle) at different microphone locations. As can be seen from the results, the simulation fits the measured spectra well, the measured trend is well captured. Again, larger deviation between the simulated and measured results occurs at 0.5 m above ground and the approximation is getting better with increasing height.

In order to have an idea of the model accuracy of each 1/3-octave band, the mean relative error between the simulation result and the measurement for each 1/3-octave band over all 27 microphone positions will be computed. To compute the mean relative error, the sound pressure level is first converted back to linear scaling

$$p(\text{Pa}) = p_0 \cdot 10^{\frac{\text{SPL}}{20}} = 2 \cdot 10^{-5} \text{ Pa} \cdot 10^{\frac{\text{SPL}}{20}}. \quad (5.1)$$

The mean relative error (MRE) is then defined as

$$\text{MRE}(p_{\text{measured}}, p_{\text{simulation}}) = \frac{1}{N} \sum_{i=0}^{N-1} \frac{|p_{\text{simulation},i} - p_{\text{measured},i}|}{|p_{\text{measured},i}|} \quad (5.2)$$

The mean relative error can also be converted to decibel using the relation

$$\text{MRE(dB)} = 20 \cdot \log_{10}(1 + \text{MRE}). \quad (5.3)$$

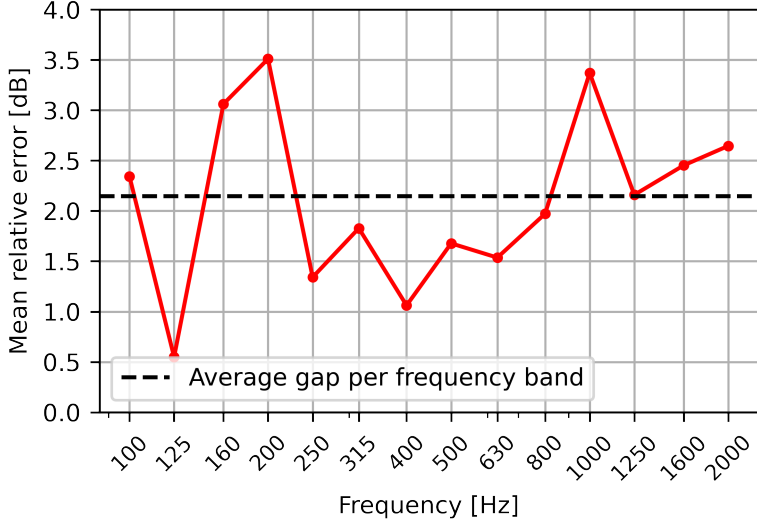


Figure 5.4: Mean relative error between simulation result and measurement for each 1/3-octave band over all 27 microphone positions

Table 5.1: Mean relative error of 1/3-octave frequency spectrum over all microphone positions

Freq (Hz)	100	125	160	200	250	315	400	500	630	800	1000	1250	1600	2000
MRE (dB)	2.34	0.55	3.06	3.51	1.34	1.82	1.06	1.67	1.53	1.97	3.36	2.15	2.45	2.65

The mean relative error in terms of the sound pressure levels over all 27 microphone positions at each frequency band between the predictions and the measurements are shown in fig. 5.4 and in tab. 5.1. As can be seen from the results, the best approximation occurs for 125 Hz band which has the smallest mean relative error among all 1/3 octave bands. Three frequency bands (160, 200 and 1000 Hz) have an error over 3 dB, and the maximum error is limited by 3.5 dB. Good approximation has also been shown for the frequency band from 250 to 800 Hz, for which the mean relative errors are within 2 dB. The average gap per frequency band is obtained by averaging the mean relative error spectrum over all 14 one-third octave bands. Following the same idea, the mean relative error in terms of overall sound pressure levels will also be used as a metric for model accuracy.

The average gap per frequency band and the mean relative error of overall sound pressure levels over all microphone positions are shown in tab. 5.2.

Table 5.2: Average gap per frequency band and mean relative error of overall SPL of initial model

Average gap per frequency band (dB)	Mean relative error of overall SPL (dB)
$2.14 \pm 1$	$0.73 \pm 0.86$

The average difference per frequency band is 2.14 dB and the mean relative error of overall sound pressure level is 0.73 dB. From these results it can be concluded that the finite element model is able to predict the sound transmission from the train underfloor adequately.

## 5.2 Effect of geometric variation

In this section, the results obtained by the variation analysis of underfloor geometry are shown. The geometrical models are illustrated and explained in section 4.3.1.

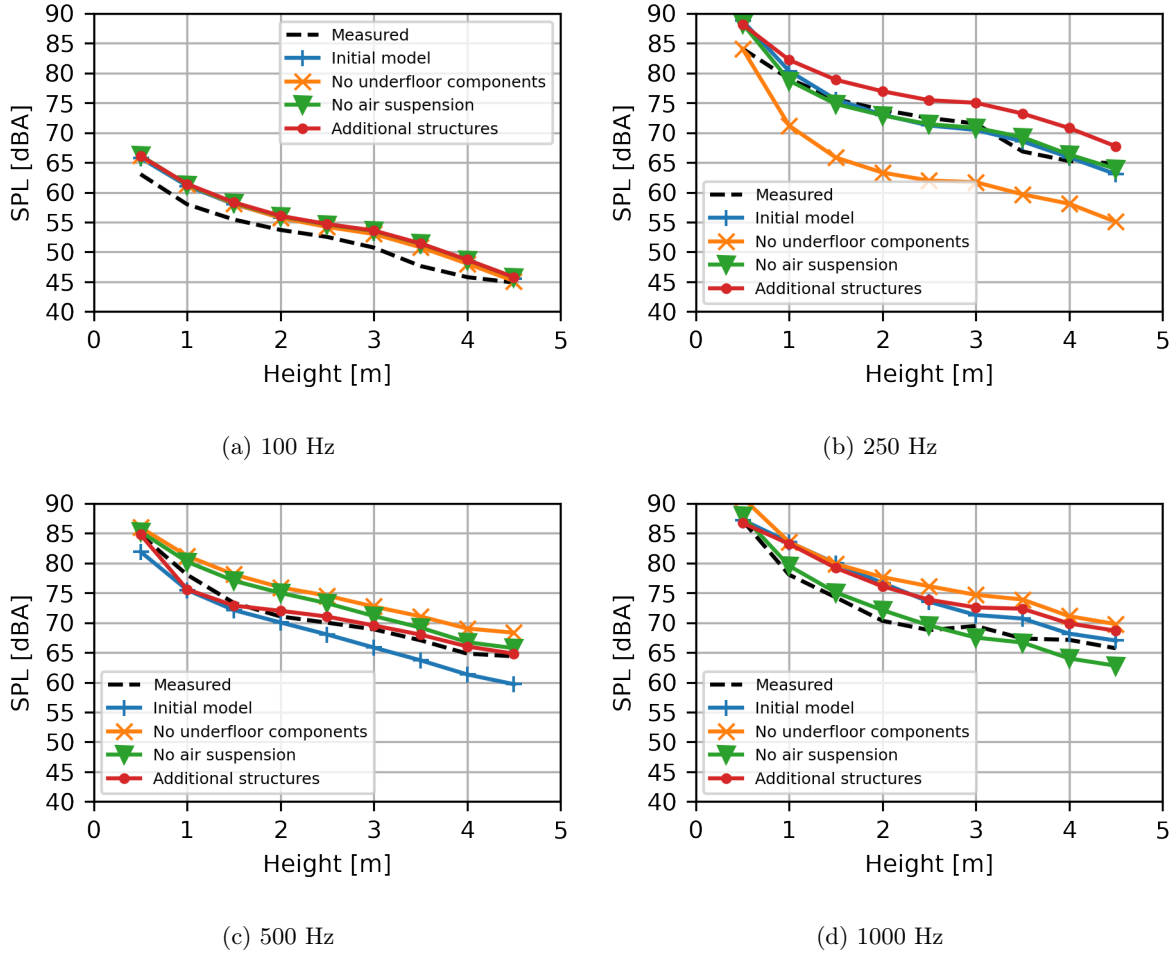


Figure 5.5: Sound distribution at measurement position a, comparison between different geometrical models with the measurements. A-weighted SPL in one-third octave bands, dBA ref 20  $\mu$ Pa.

Fig. 5.5 shows the A-weighted sound pressure level at measurement position a (10 cm away from vehicle) for different geometry variations in example one third octave bands. As can be seen from the results, at the lowest frequency band (100 Hz), there is almost no difference between the different models. This may due to the much larger wavelength (about 3.43 meter for 100 Hz) than the physical dimension of the geometry. At this frequency, all four models overestimate the sound pressure level by about 3 dB but are still able to capture the measured curve shape well. Large deviation between the models is found at 250 Hz, where the model without underfloor components shows a huge underestimation of the result and the model with additional structures tends to overestimate while the initial model and the model without air suspension are showing very good agreement with the measurement data. For 500 Hz and 1000 Hz, the model with additional structures and the model without air suspension are closest to the measurement data, respectively. In general, all models show similar shape as the measurement curves, the differences in terms of sound pressure level between the four models are within 10 dB. The same results are also observed for other frequency bands.

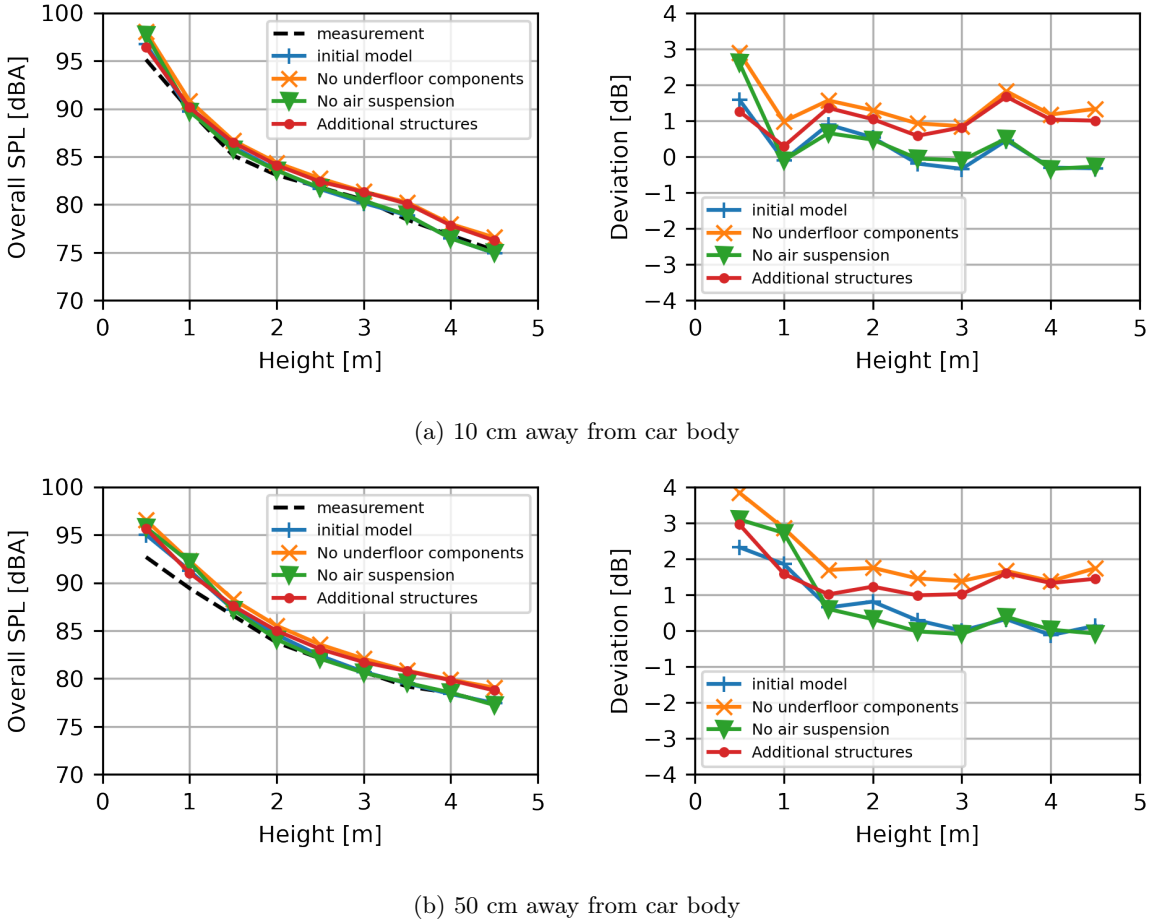


Figure 5.6: Comparison of overall A-weighted SPL for different geometrical models. Left: overall SPL as a function of height at various measurement positions. Right: difference between simulation and measurement results.

Fig. 5.6 shows the distribution of A-weighted overall sound pressure level at different distances from car body for different geometrical models. The difference between the simulation and the measurement results are plotted in the figures right. As can be seen from the figures, all four models show similar results in the lower area (up to 2 m height), deviation between the models starts to grow with increasing height. Comparing the initial model and the model without air suspension, the model without air suspension shows greater overestimation of the overall SPL than the initial model, at the height of bogie (0.5 m). Up from 1.5 m height, both models show very good agreement with the measurement results and there is almost no difference between both models. One can also see, without including any underfloor components into the model, the overall SPL is overestimated at each measurement location due to a lack of attenuation of the acoustic wave by the underfloor components. The difference between the initial model and the model without underfloor components is about 1 to 1.5 dB depending on the measurement locations. The model with additional underfloor structures shows a similar result as the initial model at 0.5 m height, but in the higher region (up from 1.5 m), the result converges to that of the model without underfloor components.

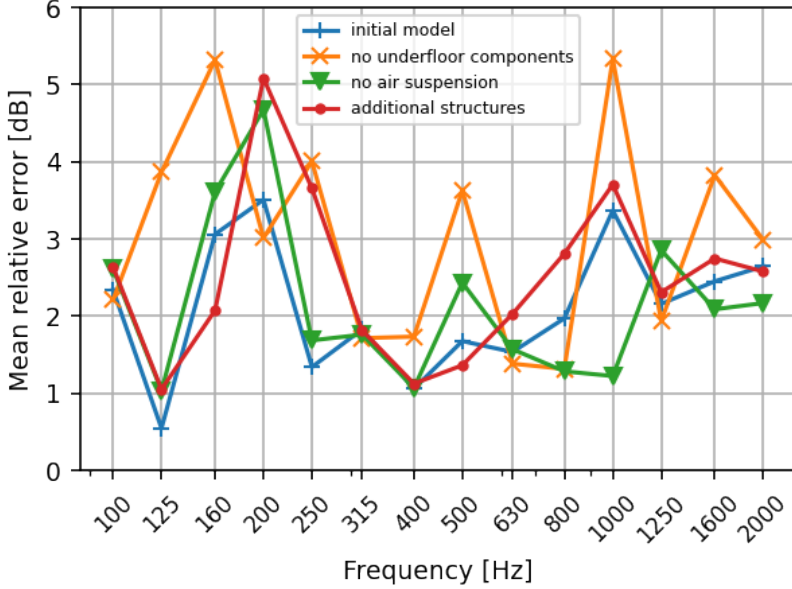


Figure 5.7: Mean relative error of 1/3-octave frequency

Fig. 5.7 shows the mean relative error spectra for the four geometrical models over all 27 microphone locations, the spectrum of the initial model has also been shown in fig. 5.4. As can be seen from the figure, all three geometry variations show greater maximum error than the initial model. For a large part of the frequency bands, the model without underfloor components has the greatest deviation among the models. At frequency band 100, 315, 400, 630 and 2000 Hz, the difference in terms of the mean relative error among the models is small and limited by 1 dB. The initial model and the model without air suspension share similar results, but at frequency band 800, 1000, 1600 and 2000 Hz, the latter model shows better approximation than the former.

Table 5.3: Average gap per frequency band and mean relative error in overall SPL for different geometry variations

Geometry name	Average gap per frequency band (dB)	MRE overall SPL (dB)
No underfloor components	$3.12 \pm 1.74$	$1.78 \pm 0.91$
No air suspension	$2.21 \pm 1.27$	$0.85 \pm 1.05$
Initial model	$2.34 \pm 1.00$	$0.73 \pm 0.86$
With additional structures	$2.57 \pm 1.38$	$1.30 \pm 0.76$

In order to quantify the difference between the geometry variations, the average gap per frequency band and the mean relative error in terms of overall SPL are computed and shown in tab. 5.3. The table is ordered by the complexity of the modeled geometry. As can be seen from results, the simplest model, namely the model without any underfloor components, shows the greatest average gap per frequency band as well as the largest mean relative error in terms of the overall sound pressure level. Both errors are reduced by almost 1 dB by including the most essential underfloor components (bogie and wheel) into the model. Taking the air suspension into account leads to a better approximation for the overall SPL, but a slightly increased average gap per frequency band, which may due to the sound hard assumption of the air suspension surface. Surprisingly, the model with additional structures shows a greater deviation in both metrics compared to the initial model. It was expected that including more underfloor details will also lead to a better approximation of the measurement. It can be concluded from the results shown in

this section that the number of modeled underfloor components do affect the prediction accuracy of the finite element model. To achieve better approximation of the measurement data, at least the bogie and the wheel should be taken into the geometrical model. Without modeling the underfloor components, the overall SPL is overestimated by about 1 dB compared to the model with underfloor components.

### 5.3 Effect of ground absorption

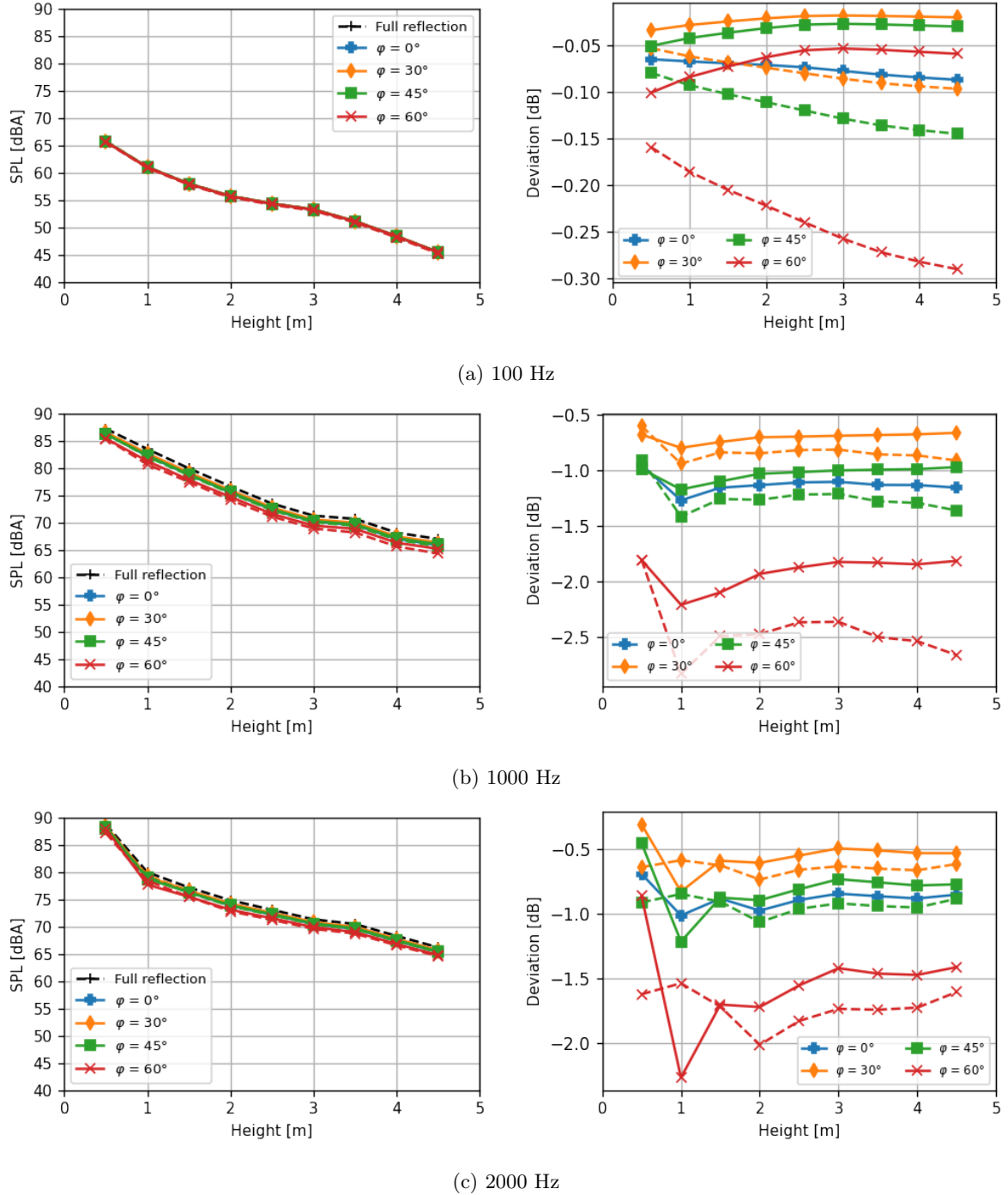
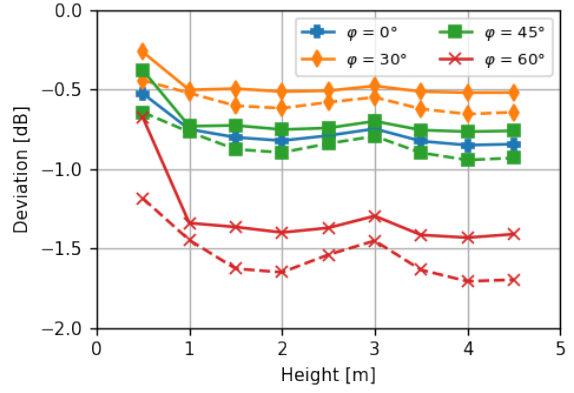
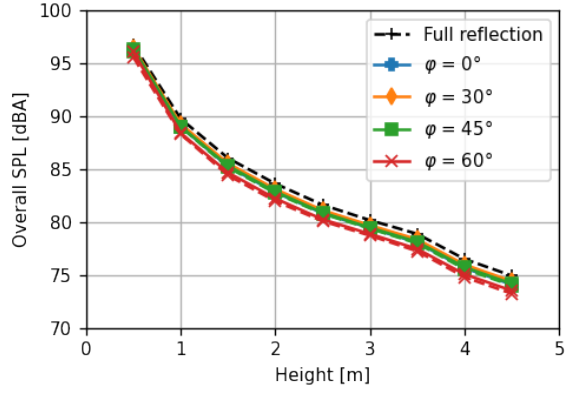
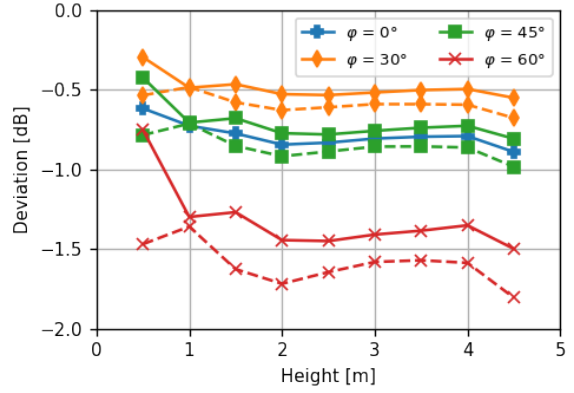
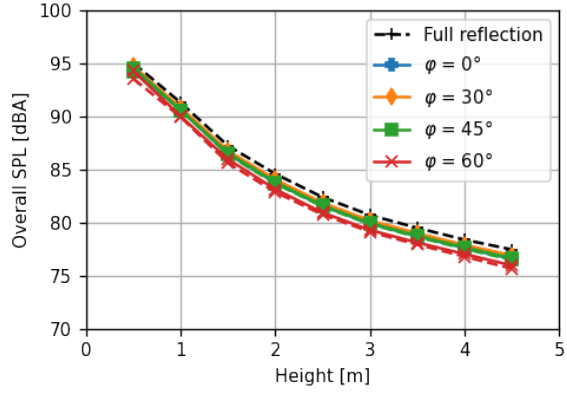


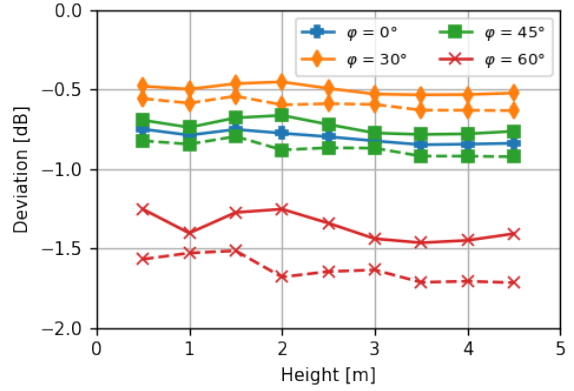
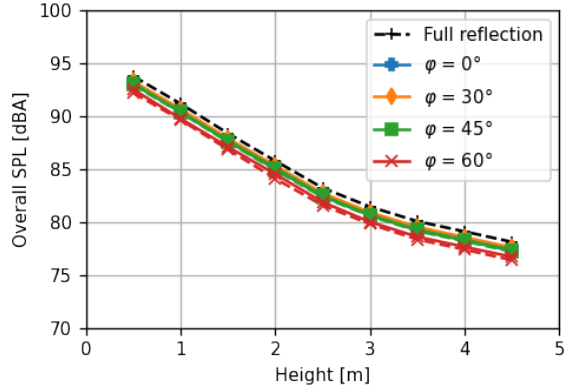
Figure 5.8: Sound distribution at measurement position a, comparison between predictions obtained from the initial finite element model with the measurements. A-weighted SPL in one-third octave bands, dBA ref 20  $\mu$ Pa.



(a) 10 cm away from carbody



(b) 50 cm away from carbody



(c) 100 cm away from carbody

Figure 5.9: Sound distribution at measurement position a, comparison between predictions obtained from the initial finite element model with the measurements. A-weighted SPL in one-third octave bands, dBA ref 20  $\mu$ Pa.

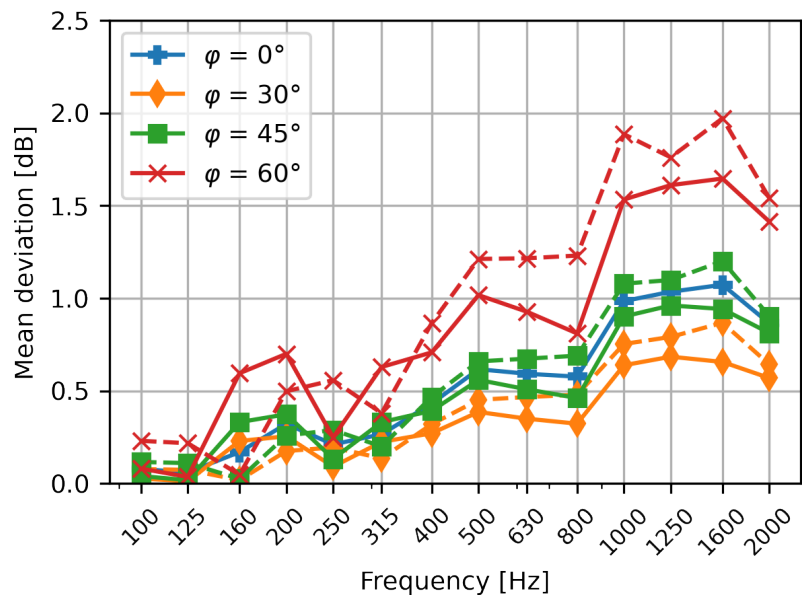


Figure 5.10: Mean relative error compared to full reflective model in 1/3-octave band

## 5.4 Effect of varying frequency steps per 1/3-octave band

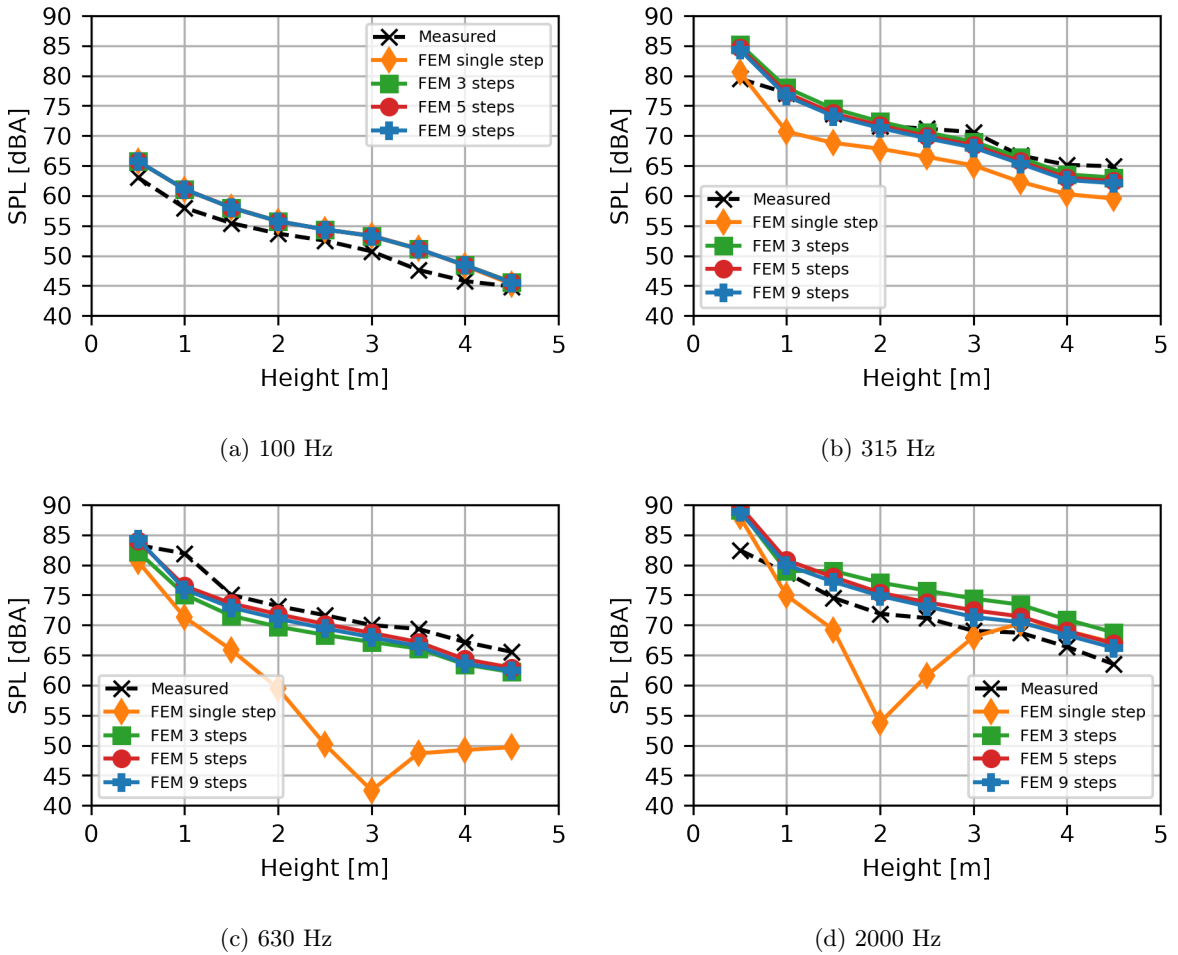
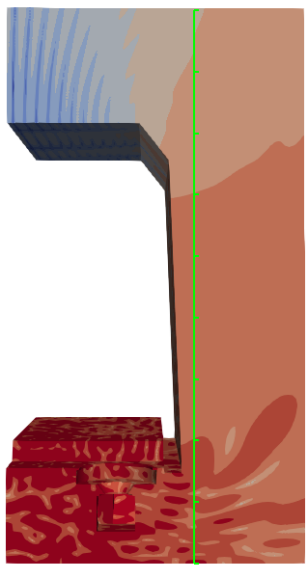
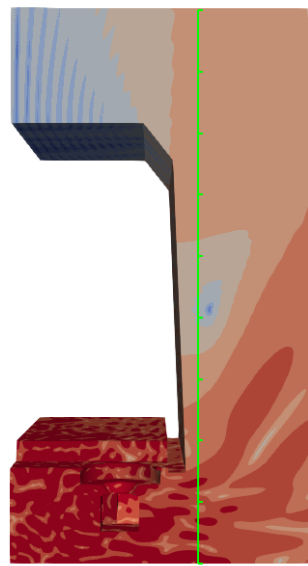


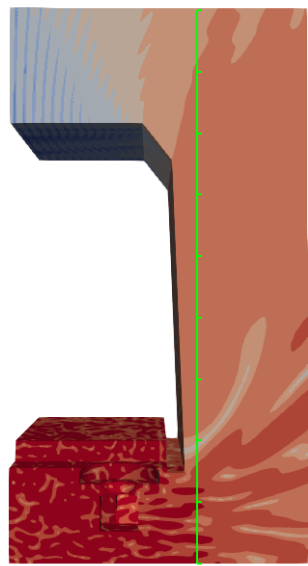
Figure 5.11: Sound distribution at measurement position a, comparison between predictions obtained from the initial finite element model with the measurements. A-weighted SPL in one-third octave bands, dB(A) ref 20  $\mu$ Pa.



(a) 1781 Hz



(b) 2000 Hz



(c) 2245 Hz

Figure 5.12: Pressure field of single frequency

# Chapter 6

## Summary and future works

In this thesis, a finite element model that is capable to predict the noise propagation from underfloor area into the exterior is developed. Validation against outer field pressure measurement shows a good agreement between the numerical results and the measurement results. The mean relative error of the overall sound pressure levels of the FE model is about 0.7 dB and average gap per one third frequency band is about 2.4 dB. The necessary propagation domain size combining good accuracy and lower computational effort is determined. It can be showed that the domain width has a greater impact for higher frequency.

The computation time for all 14 one-third octave bands from 100 to 2000 Hz with 9 intermediate frequency steps is about 26 hours using 16 cores, whereby the computation of the highest frequency band takes almost half of the total computation time (12 hours). The peak memory requirement is about 260 GB.

The number of included underfloor components in the geometry do affect the numerical results. The model without any underfloor components overestimates the overall sound pressure levels by about 1 dB compared to the model with all essential components.

If the impedance characteristic of the surface is unknown, namely that only the normal incident absorption coefficient is given, the surface impedance can assume to be real. Same assumption has been used by Li et al. [2] in their FE simulation.

# List of Figures

1.1	Transmission path of exterior noise sources [3] . . . . .	1
3.1	Setup for sound power measurement . . . . .	6
3.2	Signal generator and amplifier . . . . .	6
3.3	Scan method according to ISO 9614-2 [4] . . . . .	7
3.4	Sound power spectra in 1/3-Octave band . . . . .	9
3.5	Outer pressure field measurement setup . . . . .	11
3.6	Loudspeaker locations . . . . .	11
3.7	Measurement positions of microphone array . . . . .	12
3.8	Measurement data at position a, microphone 1 (0.5 m), loudspeaker front . . . . .	13
3.9	FFT parameter used . . . . .	14
3.10	Pressure field around carbody . . . . .	14
3.11	Total SPL as a function of the height above ground . . . . .	15
3.12	SPL as a function of the height above ground, single-frequency, measurement position a, loudspeaker rear . . . . .	16
3.13	Pressure field of 1/24-octave frequency 1000 Hz, loudspeaker rear . . . . .	17
4.1	Side view of UBX, red box indicates the modeling area . . . . .	18
4.2	Geometry of model . . . . .	19
4.3	Acoustic region . . . . .	19
4.4	Models with different simulation domain size . . . . .	20
4.5	Input surface normal velocity in dB ref. $5 \cdot 10^{-8}$ m/s, calculated using 4.12 . . . . .	23
4.6	Used geometry . . . . .	24
4.7	Absorption coefficient in one-third octave bands [8] . . . . .	25
4.8	Input surface impedance in one-third octave bands calculated using (4.16) . . . . .	26
5.1	Sound distribution at measurement position a, comparison between predictions obtained from the initial finite element model with the measurements. A-weighted SPL in one-third octave bands, dBA ref 20 $\mu$ Pa. . . . .	27
5.2	Comparison of overall SPL in dBA ref 20 $\mu$ Pa. Left: overall SPL as a function of height at various measurement positions (dashed curves: measurement; solid curves: simulation) Right: deviation between simulation and measurement results . . . . .	28
5.3	1/3-octave spectra of the A-weighted SPL for simulation and measurement data at selected microphone positions . . . . .	29
5.4	Mean relative error between simulation result and measurement for each 1/3-octave band over all 27 microphone positions . . . . .	30
5.5	Sound distribution at measurement position a, comparison between different geometrical models with the measurements. A-weighted SPL in one-third octave bands, dBA ref 20 $\mu$ Pa. . . . .	31

5.6	Comparison of overall A-weighted SPL for different geometrical models. Left: overall SPL as a function of height at various measurement positions. Right: difference between simulation and measurement results. . . . .	32
5.7	Mean relative error of 1/3-octave frequency . . . . .	33
5.8	Sound distribution at measurement position a, comparison between predictions obtained from the initial finite element model with the measurements. A-weighted SPL in one-third octave bands, dBA ref 20 $\mu$ Pa. . . . .	34
5.9	Sound distribution at measurement position a, comparison between predictions obtained from the initial finite element model with the measurements. A-weighted SPL in one-third octave bands, dBA ref 20 $\mu$ Pa. . . . .	35
5.10	Mean relative error compared to full reflective model in 1/3-octave band . . . . .	36
5.11	Sound distribution at measurement position a, comparison between predictions obtained from the initial finite element model with the measurements. A-weighted SPL in one-third octave bands, dBA ref 20 $\mu$ Pa. . . . .	37
5.12	Pressure field of single frequency . . . . .	38

# List of Tables

3.1	Description of measurement positions . . . . .	10
4.1	Computational effort for different 1/3-octave frequency band . . . . .	20
4.2	Material properties used for the simulation . . . . .	21
4.3	Estimated absorption coefficient from fig. 4.7, the values for frequency lower than 315 Hz are chosen arbitrary . . . . .	25
5.1	Mean relative error of 1/3-octave frequency spectrum over all microphone positions . . . . .	30
5.2	Average gap per frequency band and mean relative error of overall SPL of initial model . .	30
5.3	Average gap per frequency band and mean relative error in overall SPL for different geom- etry variations . . . . .	33

# Bibliography

- [1] Ilona Paozalyte, Raimondas Grubliauskas, and Petras Vaitiekūnas. Research of railway noise pollution at the living area of railway station in Klaipeda City and designing of noise barrier. *Vilnius Gediminas Technical University*, January 2011.
- [2] Hui Li, David Thompson, and Giacomo Squicciarini. A 2.5D acoustic finite element method applied to railway acoustics. *Applied Acoustics*, 182:108270, November 2021.
- [3] Jie Zhang, Xinbiao Xiao, Xiaozhen Sheng, and Zhihui Li. Sound Source Localisation for a High-Speed Train and Its Transfer Path to Interior Noise. *Chinese Journal of Mechanical Engineering*, 32(1):59, December 2019.
- [4] DIN EN ISO. 9614-2: Bestimmung der Schalleistungspegel von Geräuschquellen durch Schallintensitätsmessungen, Teil 2: Messung mit kontinuierlicher Abtastung. *Brüssel: CEN*, 1996.
- [5] Finn Jacobsen and Hans-Elias Bree. A comparison of two different sound intensity measurement principles. *Journal of The Acoustical Society of America*, 118, 09 2005.
- [6] Giovanni Moschioni, Bortolino Saggin, and Marco Tarabini. 3-d sound intensity measurements: Accuracy enhancements with virtual-instrument-based technology. *IEEE Transactions on Instrumentation and Measurement*, 57(9):1820–1829, 2008.
- [7] openCFS. openCFS. <https://opencfs.org/>, 2022.
- [8] Andrew F. Seybert and Jun xia Han. Measurement of pavement absorption using iso 13472-2. *Journal of the Acoustical Society of America*, 123:3686–3686, 2008.